DIGITAL ACCESS TO SCHOLARSHIP AT HARVARD
DASH.HARVARD.EDU

HARVARD LIBRARY
Office for Scholarly Communication

Nanopatterning and Transport Properties of Cuprate Superconductors

Citation
Litombe, Nicholas E. 2015. Nanopatterning and Transport Properties of Cuprate Superconductors. Doctoral dissertation, Harvard University, Graduate School of Arts & Sciences.

Permanent link
http://nrs.harvard.edu/urn-3:HUL.InstRepos:17465318

Terms of Use
This article was downloaded from Harvard University's DASH repository, and is made available under the terms and conditions applicable to Other Posted Material, as set forth at http://nrs.harvard.edu/urn-3:HUL.InstRepos:dash.current.terms-of-use#LAA

Share Your Story

The Harvard community has made this article openly available.
Please share how this access benefits you. Submit a story .

Accessibility

Nanopatterning and Transport Properties of Cuprate Superconductors

A dissertation presented
by
Nicholas Ebong-Sone Litombe
to
The School of Engineering and Applied Sciences

in partial fulfillment of the requirements
for the degree of
Doctor of Philosophy
in the subject of
Applied Physics

Harvard University
Cambridge, Massachusetts
May 2015

©2015 – Nicholas Ebong-Sone Litombe
all rights reserved.

Thesis advisor: Professor Jennifer E. Hoffman Nicholas Ebong-Sone Litombe

Nanopatterning and Transport Properties of Cuprate Superconductors

Abstract

Almost 30 years since the discovery of the copper oxide high temperature superconductors, the underlying mechanism describing their behavior continues to elude experimentalists and theorists alike. Understanding the electronic phases and various, possibly competing, orders at the nanoscale continues to be an active and hotly debated research enterprise. Tools available to probe nanoscale electronic behavior such as scanning tunneling microscopy have made tremendous strides in elucidating the nature of this high temperature superconductor ground state. Nevertheless, transport noise measurements on nanostructured cuprates, such as in nanowires, can aid in our physics understanding of nanoscale electronic degrees of freedom particularly for time dependent measurements. To carry out transport measurements on nanodevices, the technique has to be refined to obtain pristine devices where one probes the intrinsic material properties.

In this thesis, motivated by the need to understand nanoscale and fluctuating orders such as stripes and nematics, I will describe the strides made to develop the nanopatterning technology and the recipes for creating superconducting nanowire devices in our material of interest, $La_{2-x}Sr_xCuO_4$ (LSCO). LSCO was chosen for study because of: 1. its simple crystal structure containing a single copper oxygen plane and no copper oxygen chains; 2. its ability to be grown at doping concentrations spanning the entire superconducting dome from underdoped to overdoped; 3. and finally it can be synthesized into metallic and insulator bilayer heterostructures sustaining two dimensional superconductivity at their interface. I will show results of small cross-sectional nanowire structures fabricated by correctly identifying the problem, and mitigating them. I will first delineate the key elements in

the lithographic process, and identify the technical hurdles that must be overcome to pattern these nanowire structures. I find that our nanowire structures undergo incomplete superconducting transitions and therefore do not reflect intrinsic materials. By varying fabrication process parameters, in a systematic study I will show that the ion beam current during our pattern transfer step is the tunable parameter that determines the preservation of superconductivity in our LSCO nanowire devices. Ours is the first such study in the LSCO cuprate system. I will show results of small cross-sectional nanowire structures created by correctly identifying the problem, and mitigating them.

Next, I explore He^+ ion beam patterning of LSCO microbridges into nanostructures. I show tunable superconductor-insulator transition by varying the beam doses and energies of the scanning helium writes. I find topographic features resulting from high fluence doses and show dielectric constant contrasts between exposed and unexposed regions of the cuprate microbridge.

Finally, I propose a large scale patterning method for LSCO bilayers sustaining interface superconductivity, grown on vicinal substrates. I characterize critical current anisotropies as a metric of the technique and propose next steps towards obtaining pristine nanostructures that can further elucidate nanoscale electronic phases in the cuprates.

Contents

1 Introduction 1

1.1 Conventional Superconductivity 1

1.2 High-T_c, Pseudogap and Charge Ordering 5

2 Fabrication Recipe for Cuprate Nanowires 9

2.1 Introduction 9

2.2 Previous Works 10

2.3 Materials 12

2.4 Electron Beam Lithography 14

2.5 Argon Ion Milling 15

2.6 Completed Devices 17

2.7 Conclusion 18

3 Transport Properties of Nanopatterned $La_{2-x}Sr_xCuO_4$ 19

3.1 Introduction 19

3.2 Technical Hurdle 22

3.3 Stripes and Telegraph Noise: A Motivation for Nanowire Fabrication 24
3.4 Measurement in LSCO: The Noise is the Signal 26
3.5 The Importance of Ion Milling 28
3.6 Achieving Superconducting Sub-100 nm Narrow Nanowires 38
3.7 Ultra-Small Cross-sectional Nanowire 43
3.8 Conclusion 46

4 Tunnel Junctions and Nanoconstrictions Patterned by Helium Ion Beam 47
4.1 Introduction 47
4.2 Direct Patterning with a He^+ Ion Microscope 48
4.3 Towards Helium Ion Patterned Nanowires 51
4.4 Superconductor-Insulator Transition in LSCO Tunnel Junction Devices 53
4.5 Nanowire Pattern Results 57
4.6 Superconductivity in Nanoconstriction Devices 62
4.7 Conclusion 64

5 LSCO Bilayer Films On Vicinal Substrates 65
5.1 Novel Method for Nanowire Patterning: *Sunray* Geometry 66
5.2 Anisotropic Critical Currents 68
5.3 TEM Characterization 71
5.4 Engineering The Anisotropy 72
5.5 Conclusion and Future Work 74

6 Conclusion 75

Appendix A Fabrication Recipes Explored 77

A.1 Recipe for Nanowire Fabrication 77

References 85

Listing of figures

1.1 Superconductor critical temperatures over time 5

1.2 Comparison of YBCO and LSCO crystal structure 7

2.1 Typical AFM and Mutual Inductance images of LSCO films 11

2.2 (a) Recipe side view of an electron beam writer used to expose a nanowire pattern in negative resist spun atop an LSCO/LSAO substrate. (b) Unexposed resist areas are dissolved and washed away in developer solution leaving only exposed structures of cross-linked resist. (c) Pattern transfer to the thin film using the negative resist as etch mask is carried out with a dry etching Ar^{+} beam. (d) The cuprate film is etched everywhere but the masked region. (e) A stand-alone thin film pattern remains upon dissolving resist mask in solvent. 13

2.3 SEM image of a completed device. The voltage electrodes are seen at the center of the image while current is sourced from the larger electrodes seen here. Note the pristine nature of the sample surface of the insulating substrate. 17

3.1 Representative R(T) curve for an underdoped nanowire displaying incomplete SC transition 22

3.2 Table of SEM damage of nanowires 23
3.3 Stripe domain schematic 25
3.4 Resistance fluctuations observed in a YBCO nanowire 26
3.5 Noise data for LSCO Nanobridge at T = 41 K 27
3.6 R(T) curves for 20ML optimally doped sample with 25 mA beam current etch . . 29
3.7 Bilayer resistance vs. temperature nanowire measurements 33
3.8 Current-voltage measurement for a 14.5 nm thick LSCO underdoped nanowire 130 nm wide with doping x=0.11. This I-V shows non-linear behavior reminiscent of a completely superconducting device. The inset shows resistance versus temperature zoom for the same device showing a residual resistance of 9 Ω. The RT curve in the inset was measured with 100nA bias. 36
3.9 The Chalmers milling system adapted from an Oxford Ion Beam Etching tool . . . 39
3.10 Scanning electron micrograph of 80 nm LSCO nanowire 40
3.11 (a) Resistance versus temperature measurements for nanowires in the mesoscopic regime show comparable critical temperatures across different widths. For easier comparison,all devices shown here were patterned on the same optimally doped film with a thickness of 19.8 nm. A 100nA bias current was used. (b) Current versus voltage plot of some of the devices shown in (a) spanning wide range in bridge width, measured at T = 4 K. 41
3.12 SIMS graph of aluminum and strontium count during etching of a bilayer sample . 44
3.13 IV for 80 nm and 130 nm wide bilayer bridges at T = 4.2 K 45
4.1 Optical image of samples mounted onto chuck in the Orion microscope. Devices were grounded by wirebonding the device contact pads to copper strip shorted to stage mount. 50

4.2 (a)Helium ion microscope image of wirebonded contacts pads. The large depth of field can be appreciated. (b) Left half device is grounded to reduce charging while the right half is floated. 51
4.3 Annotated image illustrating the nanowire pattern 52
4.4 (a) Helium ion microscope image of an unpatterned device. Au voltage electrodes flank the left and right of the horizontal bridge. The bilayer sample itself was coated with in situ Au post growth for protection and to mitigate charging during Helium ion writing. (b) At very high doses even the protective Au layer was sputtered and removed in parts of the nanowire pattern traces. Measurements were carried out both before and after Au removal. 53
4.5 An annotated helium ion image and schematic of the tunnel junction pattern . . . 55
4.6 Resistance versus temperature plots as a function line dose 56
4.7 Transport results of nanowires defined by single pass outlines 58
4.8 Box outline write data from attempt at helium nanowire writes 60
4.9 Annotated Nanoconstriction pattern defined by a helium ion beam write 61
4.10 A surprising topographic feature of a nanoconstriction device with an 80 nm gap size 62
4.11 RT, AFM, SNOM of helium gap device. Gap size 800nm 63
5.1 Sunray experiment photholithography pattern 67
5.2 Critical current anisotropy on miscut substrate 69
5.3 Resistance versus temperature and anisotropy 70
5.4 80 devices showing anisotropy 71
5.5 TEM image of sample along (110) zone axis. 72
5.6 Engineering anisotropy with Zn doping 73
A.1 Optical and SEM Images of negative tone PMMA 80

Acknowledgments

First, I would like to thank my advisor, Prof. Jenny Hoffman, for all the guidance and support she has provided me during my years in graduate school. In addition to introducing me to the stimulating and challenging field of high temperature superconductivity, she was always there to have a conversation or offer advice to move the project along. A big thank you and gratitude to my co-advisor, Prof. Ivan Bozovic, for opening up his lab to a young graduate student seeking to do a very ambitious project. Thanks for always being around to discuss physics and as well as everything else. The creativity of your ideas and your sense of humor made the process easier. Thanks to both of my advisors for your financial support over the years and the luxury of your time. I'm deeply grateful.

To my friends and colleagues in graduate school, I am appreciative of the time shared as we embarked on a common purpose of pursuing a professional goal. To Ilija, thanks for your friendship and for always being there ready to talk about anything from the silly to the serious. Thanks buddy. To Anjan and Yang, thanks for the infectious passion you displayed for physics and for being around to discuss as well as share in some jokes. To the HMSG crew: Peter, James, Sorell, Audrey, Renita - it was refreshing to have a support system early on in graduate school and our lunches were so helpful in getting into the flow of graduate school and establishing camaraderie. To brothers Deriba and Muzu-

ma, thanks for the discussions in our quest for truth and for your prayers and well-wishes for my well being. I also appreciate other friends during graduate school including Jonah Waissman, Dr. Esole and Henri Baniakina.

I appreciate the time spent with all the roommates of Winslow ave. A special thanks to Lee and Joe. Kenny - it was such a pleasant surprise finding out you were moving to Boston as well. Thanks to Mr. Tanyi for our conversations. To Alice and Igor, thanks for your friendship and congratulations on your baby girl. Thanks to the rest of the Columbia crew for the relentless friendship over the years: Ling, Ron, baby Max, Kevin, Cornwall, Shanan and so many others too long a list to complete but thank you. Osekre, Alex Tsado and Kwaku - looking forward to more time hanging out. RIP Dapo. My colleagues and friends at Brookhaven who have been great sounding boards for physics and life questions. Dr. Tony Bollinger, who is a maestro in the cleanroom and always ensured its smooth running - you have been more than awesome. Thanks for your kindness. Much thanks to Drs. Leng, Wu, Pereiro, Dubuis, Strle, Sun, He for all the time spent. Lauri Peragine, I appreciate you being so welcoming and friendly. Eileen Levine has proven to be reliable and helpful in navigating BNL and having the time always to answer my questions. Thanks Barbara Drauschke for all you do. Prof. Tafuri and Dr. Massarotti, who were willing and friendly collaborators - I look forward to visiting you again. Dr. Hagsberg for our ion milling discussions and to Chuong, John and Bernhard at Zeiss for making yourselves available as we explored helium ion beam patterning.

Steve and Monique, you are the best! Li, you are an inspiration. Grandma, I wish you were here. To my brothers and sisters in Texas and abroad: Honest, Bonaventure, Laureate, Sone, Minerva, Cynthia and all of my family too long to list: thank you! Papa and Mami, thanks for always being there for me, I love you both. And above all, my mother, Edith Sone (Anzou) has been my biggest cheerleader and motivator. Thank you mom for always believing in me and for your unconditional love. We've come a long way. This thesis is dedicated to you. Love you.

1

Introduction

1.1 Conventional Superconductivity

The phenomenon of superconductivity continues to be one of the more intriguing effects observed in condensed matter systems. Since its discovery in 1911, by Karmelingh Onnes[1], its incarnation in the complex oxide Perovskites and other unconventional structures have continued to be make the topic a thoroughly active field of research. Karmelingh Onnes sought to answer the question of what

happens to the resistance of materials when cooled temperatures only a few degrees above absolute zero: that is, when many degrees of freedom have been frozen out in the physical system.

Theories at the time suggested a several available scenarios: 1. There would be an upturn in the resistivity at low temperature ultimately yielding insulating behavior for materials when cooled close to absolute zero; 2. the resistance plateaus to a low limit related to an intrinsic disorder in the system as scattering due to collective modes like phonons are inconsequential as they are frozen out at these ultra cold temperatures; 3. a linear resistance versus temperature showing metallic behavior at the lowest temperatures but with the material resistance still at a finite value. Upon measuring the resistance while cooling Hg down to $4K$, a feat predicated on the technical achievement of Helium liquefaction, Kamerlingh Onnes serendipitously measured a precipitous drop of the Hg-resistance at a temperature called the critical temperature or transition temperature, T_c, below which the resistance vanished to zero within the lowest experimental limit of the resistance measurement setup. Experiments later could measure the life time of the persistent current responsible for this superconducting state, and observed the non-attenuation of the current value in the superconductor implying a dissipation-less thermodynamic state had been achieved.

Several decades after the observation of zero resistivity in Hg through electrical conductivity measurements, Meissner and Ochsenfeld [2] in 1933, observed the effects of a magnetic field on superconductors. When a conventional Type-I superconductor is exposed to an applied external magnetic field, persistent currents within the superconductor screen out the applied field, expelling it from within the superconductor such that the magnetic induction within goes to zero. Consequently, superconductivity is more than just the portmanteau of super and conductivity. The occurrence of perfect Meissner diamagnetism in conventional superconductors is not present in a normal conductor, or even one with zero resistance. Incidentally, superconductivity is an entirely different thermodynamic state.

For so-called Type-I superconductors, which consists of mostly elemental materials and other se-

lect alloys, the externally applied field is screened up to a thermodynamic critical value of the applied field called, H_c. Below H_c, the magnetic flux is perfectly expelled implying a macroscopic average bulk magnetization of -1. Above H_c, conventional superconductor returns to the normal, resistivity state. Special cases of magnetism in conventional superconductors, particularly on surfaces, include intermediate states where domain formation exist of both superconductor and normal regions with the intervening domain walls attaining a positive free energy. That is, there's an energy cost to creating these intermediate states at the domain wall. When the free energy cost to create these domain walls surpasses that of the resistive normal state, the material goes completely normal.

Later, Abrikosov[3] predicted the existence of a new class of superconductors, Type-II, where the free energy of the domain between the normal and superconducting state was negative and thus above a critical applied magnetic field, H_{c_1}, magnetic flux would not be completely expelled but would penetrate the material in quantized vortices with magnetic flux of Φ. Below H_{c_1}, as with conventional superconductors, a magnetic field penetrates a superconductor within the penetration depth, λ. The superconductor diamagnetic response elicits screening currents within the length scale of lambda from the sample surface to cancel out the magnetic induction in the bulk of the material. The vortices in type-II superconductors consist of a normal core the size of a coherence length, ξ. The coherence length is the length scale over which the superfluid density of carriers changes and it characterizes all superconductors much like the penetration depth. The Ginzburg-Landau parameter given by,

$$\kappa = \frac{\lambda}{\xi}$$

determines whether a superconductor is Type-I vs. Type-II. For all the interesting phenomena described above about superconductors, it was until approximately four decades after Karmelingh Onnes' discovery, in 1957, that a microscopic mechanism was proposed by Bardeen, Schrieffer, Cooper: BCS theory[4]. BCS theory described the microscopic superconducting state as resulting from pair forma-

tion of electrons, called Cooper pairs, which can propagate through the lattice of ions without scattering thereby yield dissipation-less transport properties. The theory also predicted the formation of an energy gap in the density of states. Furthermore, BCS theory provided an equation for the critical temperature of these superconductors given by the formula,

$$kT_c = 1.13\hbar\omega_D exp(-\frac{1}{N_F V}) \tag{1.1}$$

Here, $N_F V$ is a product of the density of states at the Fermi level (N_F) and the electron-phonon coupling (V). This formula could not be derived by perturbative theoretical means. Furthermore, it involves the Debye frequency, ω_D of the material and in so doing implicates phonons as providing the attractive force mediating the cooper pairing of electrons. The BCS theory provided insight into the previously observed isotope effect. In addition, BCS theory[4] proposed in 1957 was a resounding success because the theory provided an explanation for the empirical hallmarks of superconductivity: zero resistance state and perfect diamagnetism corroborating experimental studies at the time. The microscopic theory proposed the symmetry of the orbital part of the anti-symmetric fermionic wavefunction was s-wave in nature and the wavefunction in the spin channel was the singlet state anti-symmetric under particle exchange and incidentally with odd parity. The isotope effect, discontinuity of the thermodynamic specific heat at the critical temperature, the high frequency optical transmission experiments[5] performed by Tinkham et. al. observed an energy gap later confirmed by the BCS microscopic theory. Tunneling experiments were carried out to further elucidate the nature of the pairing gap. Pioneering experiments of this nature were carried out by Giaever[6]. One of the more astounding predictions that come from the theory, a prediction originally discarded as nonsensical by Bardeen, was made by Brian Josephson in 1962. The Josephson effect[7] as it is now called predicts a finite critical current between two superconductors in close proximity to one another even at zero voltage bias. Typical lengths scales of the proximity are on the order of coherence lengths. The im-

portance of this effect, is its dependence on the relative phase difference of the condensate across the barrier. With fundamentally aspects of conventional superconductivity becoming more clarified, simultaneously there was a race to achieve higher and higher T_c's still, culminating in high temperature superconductivity discovery in the 1980s.

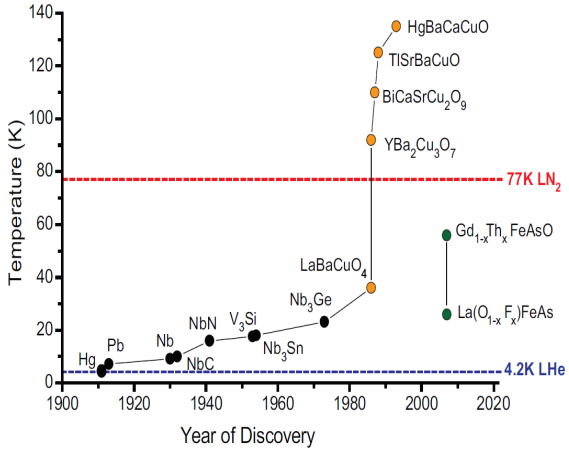

Figure 1.1: The evolution of superconductor critical temperatures over time. Orange circles mark cuprate materials and green, the pnictide compounds discovered in 2008.(Adapted from[8])

1.2 High-T_c, Pseudogap and Charge Ordering

High temperature superconductors were first synthesized in the Perovskite Ba-La-Cu-O system by Bednorz and Muller[9] in 1986 with a critical temperature in the 30 K range. A year later, the LN_2 temperature limit (T = 77 K) was surpassed by Wu et. al[10] when they synthesized the Y-Ba-Cu-O mixed phase compound with a critical temperature of T_c =93 K.

It became evident early on that the high temperature superconductors display a very rich phase diagram marked by regimes of phase transitions as well as cross overs controlled by dopant concentration (p), temperature (T), magnetic field (H) and pressure (P) in some cases. The most noticeable

transition occurs as the parent Mott insulator compound is doped with charge carriers (electrons or holes) of concentration, p, typically with oxygen or elemental substitution. With sufficient hole concentration, usually around p = 0.05, the crystal attains a superconducting state. Further doping of the material causes the superconductor critical temperature, T_c to rise until its maximum critical temperature at optimal doping, p = 0.16. Additional doping only serves to decrease T_c until it vanishes. Even after three decades, many puzzles exist in the phase diagram. In particular, the pseudogap state which is observed in the normal state and most pronounced in the region underdoped region in proximity to the anti-ferromagnetic (AF) phase. The pseudogap is aptly named as it is the partial suppression of the density of states with symmetry observed to be similar to that of the superconducting gap although it exists above T_c. While an assortment of experimental tools[11] have been levied on cracking the puzzle, It is still a hotly debated topic the exact relationship between the pseudogap state and the superconducting state. Are they separate orders competing for the same phase space ? or are they intertwined, with the pseudogap state a precursor to a formed quantum macroscopic superconducting state at T_c ? Many have attempted to answer this question of the past couple decades by exploring on the nanoscale charge ordering resulting from electronic phase separation.

Electronic phase separation runs rampant in strongly correlated material systems[12]. However, in the cuprates, the existence of electronic phase separation is still controversial and actively researched. Theories have been proposed about the nature of these purported electronic phase separated patterns. Some of the patterns proposed include so-called stripes and nematics with modulated charge and spin density atop the host crystal which have been discussed at length theoretically in a variety of incarnations in the cuprates[13,14,15]. Neutron scattering with its magnetic sensitivity has found charge order states strongest at 1/8 doping in the La-214 cuprate crystal system[3] , which can be grown large enough to produce sufficient signals needed for these neutron scattering runs. STM, a surface technique, with its atomic resolution has been used as a probe to try and make sense of the complexity and microscopic inhomogeneities which may drive these lush electronic formations, including observation of the famous

checkerboard pattern around vortex cores[16]. Big picture wise, it's not entirely electronic phase separation zoology driving these studies envelope-pushing studies. Such studies on the nanoscale have been purported to link the nanoscale electronic observations to pseudogap behavior[17] such as for stripes of the fluctuating variety and its possible link to pseudogap physics to the superconducting state. Distinguishing between different charge orders is another direction of study[18]. Recent experiments have sought to reconcile nanoscale surface observations to the bulk[19], clearing a way in which apt comparisons can be made across a variety of technique, with STM and X-ray scattering singled out here in particular.

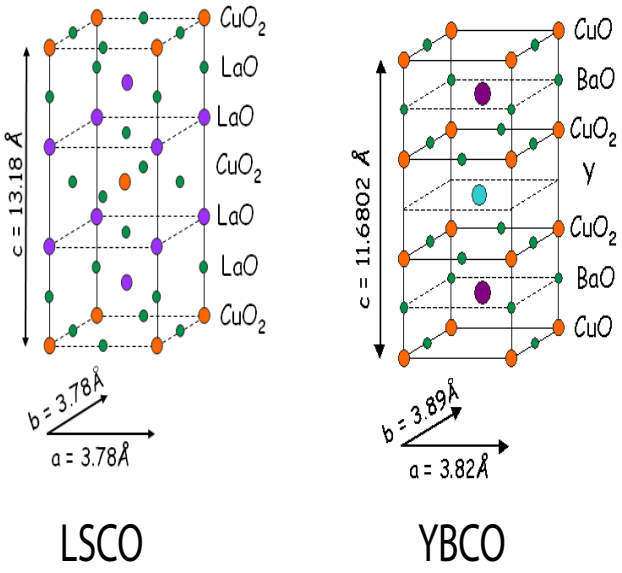

Figure 1.2: In this work we will focus on the $La_{2-x}Sr_xCuO_4$ (LSCO) system, a cousin (214-family) of the Ba-La-Cu-O compound first synthesized by Bednorz and Muller. A comparison of LSCO and $YBa_2Cu_3O_7$ (YBCO) crystal structure. LSCO contains a single copper oxygen plane as opposed to 2 planes for its YBCO counterpart. More importantly, YBCO contains Cu-O chains which also contribute to conductivity as they become more doped with oxygen: a complication not present in LSCO.

We look to study the existence of stripe-like ordering in the cuprates by transport measurements. Transport measurements are especially useful when probing time-dependent intrinsic properties of

the material. To do so, in this thesis we explore and develop the prerequisite nanopatterning techniques to create these nanostructures, thereby paving the way to carrying out transport experiments which can probe intrinsic nanoscale cuprate properties. Here, we focus on the $La_{2-x}Sr_xCuO_4$ (LSCO) system over $YBa_2Cu_3O_7$ (YBCO) because of its simpler crystal structure (Fig.1.2) lending easier interpretation to experiments of interests, growth of pristine films with doping spanning the entire dome. LSCO films with bilayer heterostructures[20], have been grown to sustain interface superconductivity: one variety of films studied in this thesis.

1.2.1 Dissertation Outline

In chapter 2, I summarize the fabrication recipe developed to tackle the challenging process of patterning cuprate materials.

In chapter 3, I describe the technical hurdle that needs to be overcome in order to create LSCO nanowires showing a complete superconducting transition. Overcoming the technical hurdle is motivated by a physics experiment that can provide key insights into the nanoscale charge ordering nature of the cuprates. Most of my thesis work was devoted to overcoming this challenge. I examine a solution to this problem and present results from the narrow nanostructures made.

In chapter 4, I explore an alternative technique for making nanowires using a Scanning Helium Ion Beam. I explore the merits and drawbacks to this technique. I propose a new method for measuring tunnel junction lateral extents by transport through nanoconstriction devices. I pattern superconducting tunnel junctions and observe topographic features from ion-sample interactions at high He^+ fluence.

In chapter 5, a unique and promising method for creating large scale nanowires and Josephson junctions using bilayer films grown on vicinal substrates is explored. I show preliminary data which will help guide the necessary next steps in refining the method.

2

Fabrication Recipe for Cuprate Nanowires

2.1 Introduction

Some of the results and text of this chapter were published under the title *$La_{2-x}Sr_xCuO_4$ superconductor nanowire devices*[21] and are repeated here. Reprinted from N. E. Litombe, A. T. Bollinger, J. E. Hoffman and I. Božović, Physica C 506, (2014) 169-173. Copyright 2014.

Most studies of low dimensional, high temperature superconducting devices have focused on nanopatterning $YBa_2Cu_3O_7$ (YBCO) cuprates[22,23,24,25,26,27,28]. Only one other thin film nanopatterning study known to the author at the time of writing has been carried out in $La_{2-x}Sr_xCuO_4$ (LSCO)[29]. Unlike purely oxygen-doped YBCO, LSCO thin films can be doped to span the entire superconducting dome from underdoped through overdoped making it crucial to explore nanofabrication technology for these class of materials. In addition, LSCO is of particular interest by virtue of its simpler crystal structure. Because of their short coherence lengths (1-4 nm), and sensitivity to disorder and stoichiometric imbalances, particularly to the loss of oxygen, fabricating nanostructures from these complex oxides has proven to be extremely challenging. The goal is to obtain critical properties in the nanostructures close to the bulk. In this chapter, I outline the recipe I developed to meet these challenges and to fabricate single nanowire and nanostructure devices from LSCO.

2.2 Previous Works

Dimension-limited superconductivity on the nanoscale can provide insights into the fundamental underpinnings of high temperature superconductivity as well as having technological ramifications for novel device architectures. Recent applications of low-dimensional superconductor devices include single-photon detectors operating at quantum efficiency[30,31] and Josephson Junctions[32] as used in voltage standards. Nonetheless, important considerations arise on the nanoscale such as the fate of superconductivity as device dimensions shrink and approach the length scales of the magnetic penetration depth and superconducting coherence length[33].

Because of longer coherence lengths, which effectively set the scale for the dimensionality of superconductivity along the narrow length of the device, nanoscale devices fabricated from conventional low-temperature superconductors have been studied intensely for several decades. In particular, phase

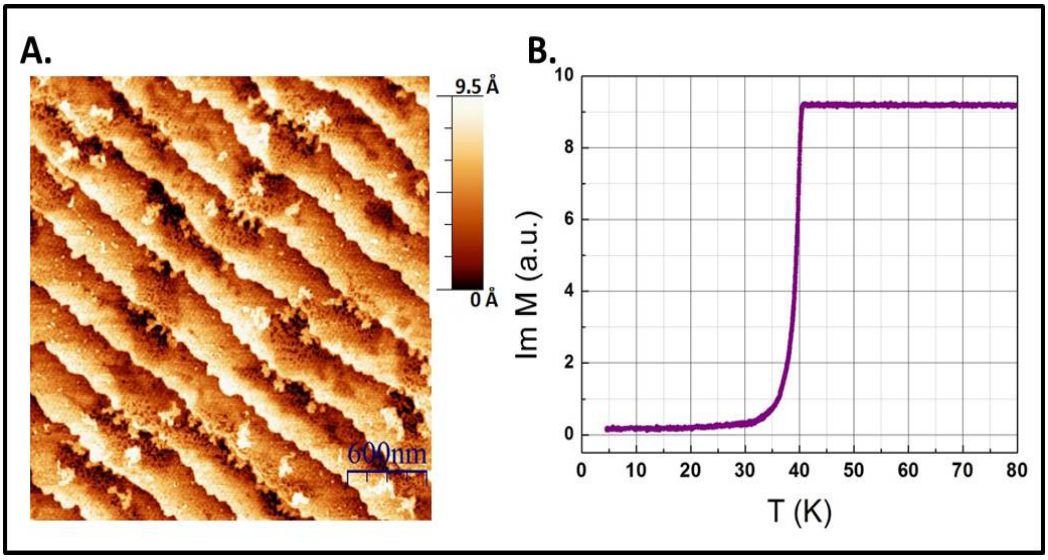

Figure 2.1: Typical AFM and mutual inductance data of LSCO films. (a) An AFM image of an ALL-MBE-grown $La_{2-x}Sr_xCuO_4$ (LSCO) film, showing the rms surface roughness less than 3 Å, over a 9 μm^2 scan area. (b) The imaginary part of the mutual inductance of an optimally doped, 20 unit cell thick LSCO film, showing $T_c = 41$ K

slips have been predicted and observed in nanowire devices of widths comparable to or smaller than the coherence length, i.e., in the quasi-1D limit[33,34,35,36]. These phase-slip events locally suppress the superconducting order parameter along a nanowire segment yielding a finite resistance even below the bulk critical temperature, T_c, and at low current bias smaller than the superconducting critical current, I_c. Although firmly established for low-temperature superconductors[36], observing phase slip processes arising from quantum fluctuations of the superconducting order parameter in cuprate superconductors remains an area of active investigation[37].

Fabricating nanowires from cuprate superconductors is advantageous because of higher T_c, higher J_c, and a larger superconducting energy gap. In previous studies, high-T_c wires were fabricated with widths ranging from micron-scale down to the sub-100 nm scale[37,23,27,28,26,22]. Other nanostructures fabricated from high-T_c materials include nanorings and nano-loop networks probing magnetoresistance oscillations[29,38]. Interesting superconductivity effects reported in $YBa_2Cu_3O_7$ nanostruc-

tures include: thermally activated phase slips[23], very high j_c values close to the Ginzburg-Landau (GL) depairing limit[23,26], anomalous magnetoresistance oscillations in nanowires[27,28] and finally, telegraph noise in the pseudogap regime ascribed to stripe domain switching[22,39]. Few studies to test the universality of these observed phenomena and their relation to the underlying mechanism of high-T_c superconductivity have been carried out using other cuprate materials[29,38].

2.3 Materials

The LSCO films were synthesized using atomic-layer-by-layer molecular beam epitaxy (ALL-MBE), on 10x10x1 mm^3 $LaSrAlO_4$ (LSAO) substrates polished perpendicular to the (001) direction. The ALL-MBE growth technique allows for digital control of the LSCO film thickness, as reported previously in the synthesis of films showing interface superconductivity[38,39]. Reflection high-energy electron diffraction (RHEED) was used to monitor film crystallinity during growth. Strong diffraction streaks were observed without any transmission spots; together with pronounced oscillations in the intensity of the specular spot, this was an indication of atomically smooth interfaces and surfaces, without any secondary precipitates. Atomic Force Microscopy (AFM) was used post-growth to characterize the surface roughness of LSCO films. Typical values of rms surface roughness observed by AFM with a 9 μm^2 scan area were in the range of 2-3 Å as seen in 2.1a. Films patterned in this study had compositions in the underdoped region ($La_{1.89}Sr_{0.11}CuO_4$ and $La_{1.90}Sr_{0.10}CuO_4$) and at the optimal doping level ($La_{1.84}Sr_{0.16}CuO_4$). For some films, the surface was protected by a 10 nm thick capping gold layer, deposited in situ. Contactless mutual inductance measurements of the sample susceptibility were carried out to determine the film's bulk T_c and transition broadness before lithographic patterning. Figure 2.1b shows typical mutual inductance data.

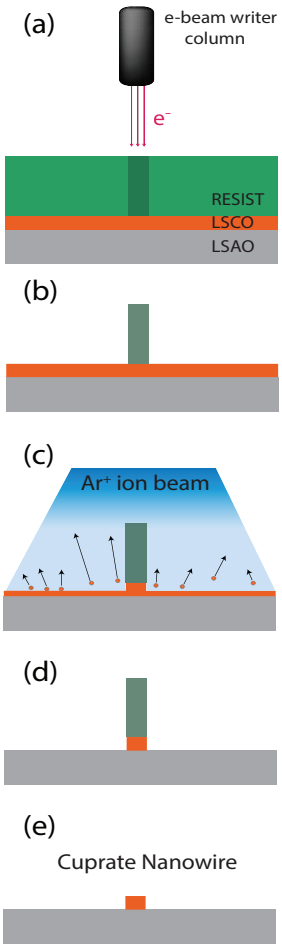

Figure 2.2: (a) Recipe side view of an electron beam writer used to expose a nanowire pattern in negative resist spun atop an LSCO/LSAO substrate. (b) Unexposed resist areas are dissolved and washed away in developer solution leaving only exposed structures of cross-linked resist. (c) Pattern transfer to the thin film using the negative resist as etch mask is carried out with a dry etching Ar^{+} beam. (d) The cuprate film is etched everywhere but the masked region. (e) A stand-alone thin film pattern remains upon dissolving resist mask in solvent.

2.4 Electron Beam Lithography

Four-point-contact cuprate nanowire devices were patterned as shown in Fig.2.2a using high-resolution electron-beam lithography (EBL). The negative-tone MA-N2401 or MA-N2403 resists was spun to a thickness ranging between 100 nm and 300 nm and exposed in an electron beam writer (Fig.2.2a). T-wo writers, JEOL 6300FS and an FEI Helios dual beam NPGS, were used for EBL patterning with accelerating voltages of 10 kV - 30 kV and 100 kV, respectively. The JEOL 6300FS writer has an overlay accuracy of less than or equal to 20 nm and a field stitching accuracy of 20 nm. High resolution patterning for the JEOL for smaller features can be carried in a mode 6 exposure using a field size of 62.5 μm x 62.5 μm. Low resolution writes relative to mode 6 are performed in mode 3 operation of the instrument with a larger write field than mode 6, of approximately 1 mm by 1 mm. The FEI Helios was used for low voltage exposures and relies on an nanometer pattern generation system (NPGS) system for patterning.

Efficient exposures of the nanowire patterns relied on utilizing two current write procedures. Beam currents 25 pA - 850 pA were used to write nano-features ranging from 80 nm to 2 μm widths, while large contact-pad patterns were exposed using larger currents, between 1 nA and 4 nA, with EBL accelerating voltage-dependent beam doses of 50 - 120 μC/cm^2. Drift compensation available for both the JEOL and the FEI instruments allowed for correction upon switching between high and low beam currents.

For negative-tone resists, in areas exposed to the electron-beam flux, the resist cross-links, and becomes resilient to the developer. Unexposed regions are washed away by the developer solution (Fig.2.2b) . The cross-linked negative-tone resist pattern serves as an etch mask in a subsequent pattern transfer step. Several other resists and e-beam recipes were explored in the course of this study including: positive PMMA for lift-off, tone-reversal PMMA as another negative tone etch mask, and HSQ for pattern transfer to a carbon underlayer using reactive ion etching (RIE). Most of the devices

discussed will be those patterned using the negative tone MAN-2400 series.

2.5 Argon Ion Milling

Patterns exposed in electron beam resist were transferred down to the LSCO film and through to the LSAO substrate using an Ar^+ milling process (2.2c). Ar^+ beam etching or ion milling, an ion equivalent of sandblasting, is an entirely physical system which possesses great directionality. Due to ion milling being a physical process it incidentally has poor selectivity between target materials. Cuprate films do not form volatile compounds in most reactive gases, rendering the ability to selectively etch the cuprate oxide and not the resist or metal etch mask, difficult if not impossible. In the semiconductor community for example, reactive ion etch processes are very common thereby improving the aspect ratios of etched structures. The reliance of cuprate fabrication on ion milling as a pattern transfer tool is the principal practical difficulty in making these materials amenable to conventional fabrication procedures.

Prior studies on cuprate nanofabrication have used hard masks such as carbon or titanium. Carbon and titanium both have a low etch rate compared to the cuprate and implementing these masks allows for etching thicker cuprate films. The carbon fabrication technique has been used by several groups to successfully pattern transfer. However, using a carbon mask necessitates a reactive ion etching step and a metal layer atop the carbon for pattern transfer. A lift-off process is often needed to deposit the metal layer atop the carbon and a protective shield in the discriminating RIE step. For titanium hard marks, their removal is not so easy. Buffered HF solutions can be used to strip titanium above the cuprate nanodevices post-ion milling. The drawback in doing this is a potential destruction or damage to the cuprate film.

Our technique of using a negative tone resist makes the lithographic process more streamlined. While not as hard a mask as either carbon or titanium, it can be successfully used to pattern thin-

ner films. Striping the e-beam resist is also seamless. This is done in a solvent which does not cause observable harm to the cuprate nanodevice. We carried out tests by soaking samples in solvents and measuring mutual inductance of the film after.

Mitigating heating is crucial in the pattern transfer process as previous studies of sample annealing in vacuum have shown the development of multiple peaks in mutual inductance; indicating cuprate film sensitivity to high temperatures. Films were ion-milled on either a liquid nitrogen-cooled or a water-cooled stage to reduce sample damage during ion milling. For Au-capped devices whose intrinsic properties we intended to characterize above T_c, a second EBL step was performed to remove the Au-cap. For the second EBL, we used alignment marks defined in the first beam exposure to open up a window in the positive PMMA resist only atop a segment of the nanowire. A quick etching step with a Au-etchant (potassium iodide diluted with water) solution was then used to remove the Au parallel resistance, thus allowing for measurements of the bare LSCO devices.

Because Ar^+ milling proved to be pivotal in nanowire fabrication we explored several ion beam etching parameters to fine tune the fidelity of nanostructures produced. Ion beam voltages used for fabrication ranged from 310 V - 1 kV and beam current values from 5 mA to 50 mA. The source diameter for the ion milling system which informs the Ar^+ beam current density was also taken into consideration and varied since the beam current density controls the magnitude of current at the sample. Finally, some samples were attached to either liquid nitrogen or water-cooled stages with the beam duty cycle varied from 20 s and even up to continuous runs. To determine the appropriate stoppage time for the milling step, SIMS endpoint detectors were used in fabricating some subset of samples. In this way, were explored the ion beam etching parameter to optimize for fabricating pristine electronic nanostructures.

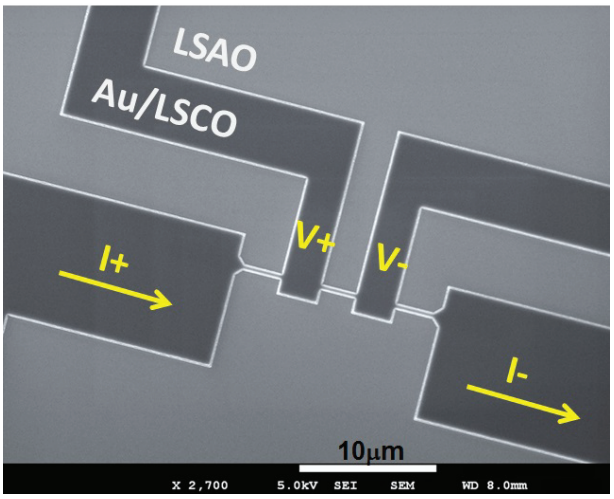

Figure 2.3: SEM image of a completed device. The voltage electrodes are seen at the center of the image while current is sourced from the larger electrodes seen here. Note the pristine nature of the sample surface of the insulating substrate.

2.6 Completed Devices

We used a scanning electron microscope (SEM) to image nanowire devices, and measure their line widths. Fig.2.3 shows a typical Au-capped single nanowire where the current source-drain and voltage leads are made of the same LSCO film as the nanowire in order to avoid contact-resistance issues that sometime arise for interfaces between high-T_c superconductors and common metals. In Fig.2.3, the voltage drop is measured across a nanowire segment of length 2.5 μm. The device seen in Fig.2.3 is still protected by a negative-tone resist etch mask. Beneath the resist mask are layers of Au and LSCO for this particular device. The larger electrodes are used to source current through the nanobridge. Everywhere beyond the pattern is the etched LSAO substrate.

2.7 Conclusion

In this chapter I have outlined a high resolution electron beam lithography recipe I developed to pattern cuprate nanowires on the nanoscale. For the remainder of the thesis, the nanowires patterned were carried out following this recipe.

3

Transport Properties of Nanopatterned $La_{2-x}Sr_xCuO_4$

3.1 Introduction

Some of the results and text of this chapter were published under the title *$La_{2-x}Sr_xCuO_4$ superconductor nanowire devices*[21] and are repeated here. Reprinted from N. E. Litombe, A. T. Bollinger, J.

E. Hoffman and I. Božović, Physica C 506, (2014) 169-173. Copyright 2014. Results and text of this chapter are also in preparation for publication in a manuscript[40] titled *Mesoscopic Properties of Superconducting Lanthanum Cuprate Nanowires* (N. E. Litombe, D. Massarotti, A. T. Bollinger, F. Tafuri, X. He, I. Božović, and J. E. Hoffman)

Low dimensional devices patterned from high temperature cuprate superconductors provide a direct means to test some of the bedrock principles fundamental to understanding the high temperature superconductor problem. The fate of superconductivity during the process of dimension reduction from the native 3D bulk material, through one dimensional (1D) nanowires, and ultimately down to zero dimensional quantum dots, provides us with exemplars of of understanding that could elucidate a core principle at work in these strongly correlated systems. Different excitations that suppress superconductivity begin to play a dominant role at each successive step in reducing the system dimension and length scales: vortex excitations in 2D, phase slip lines and phase centers in one dimensional wires and finally charging energy costs can compete with and dominate the Josephson energy in 0D, giving rise to parity effects at very low temperatures. Technological applications of superconductor electronics such as in Josephson junctions used in voltage standards, SQUID magnetometers, single photon detectors[30,31] may be limited by these excitations that suppress superconductivity at smaller length scales. Engineering better superconductor nanoscale devices operating at quantum efficiency[30] relies on both a refined patterning technology and consequently a better understanding of the processes at work with reduced superconductor dimensions and length scales.

Predominantly because of their higher critical temperature, extensive explorations of quasi-1D cuprate nanowires have been carried out in the Yttrium-based cuprate, $YBa_2Cu_3O_7$ (YBCO), doped solely with oxygen. Although YBCO has a higher critical temperature, YBCO has a more complicated

crystal structure involving copper-oxygen chains and multiple copper-oxygen planes that may be a drawback in interpreting data in some experiments. More importantly, YBCO thin films doped solely by oxygen are limited in their span of the superconducting dome. These films can be doped from the underdoped, through optimally doped regions but not extensively beyond optimal doping point. The overdoped region is not wholly accessible. From the perspective of studying quantum critical points which influence superconductivity, this can be a limitation. In contrast to YBCO however, the lanthanum cuprate 214-family of superconductors, contains a single copper oxygen plane. An elemental dopant (Sr,Ba) replacing Lanthanum allows the system to span the superconducting dome from underdoped, through optimal doping,and into the overdoped region and beyond.

3.1.1 Summary of Chapter Results

In this chapter, we have grown LSCO films on LSAO substrates by ALL-MBE, and patterned them into four-terminal devices with widths down to 80 nm. The critical technical hurdle was that nanowires tended to show non-zero residual resistance and incomplete superconducting transitions. These residual resistances limited the minimal width of superconducting nanowire devices that could be fabricated using this recipe. We tracked the underlying cause of the incomplete superconducting transition to the sensitivity of cuprate films to damage by electron and ion beams, to which they were exposed in the nanowire fabrication process. We took additional measures, particularly during ion-milling, to minimize the film damage during these process steps, such as utilizing liquid-nitrogen cooling of the sample stage and reduction of the ion-milling beam voltages and current. Subsequently, we observed complete superconducting transitions in nanowires down to 80 nm wide for both 19.8 nm thick optimally doped films and 10M + 10I bilayer films. We report for the first time the fabrication of an ultra-small cross-sectional nanowire in the LSCO bilayer sustaining interface superconducting. The cross section of the nanowire is 80 nm x 0.66 nm with a cross sectional area of 53 nm^2 and a critical current density > 10^7 A/cm^2[25].

3.2 Technical Hurdle

Hundreds of nanowires were fabricated and measured for this thesis. As described in chapter 2, the argon ion milling step is used for pattern transfer through to the cuprate. Our initial fabrication procedures used ion milling voltages of 500 V - 1 kV and ion beam current of 50 mA over a 5 cm diameter DC Kaufman source. For each nanowire fabricated with those high ion beam parameters, we measured the resistive transitions.

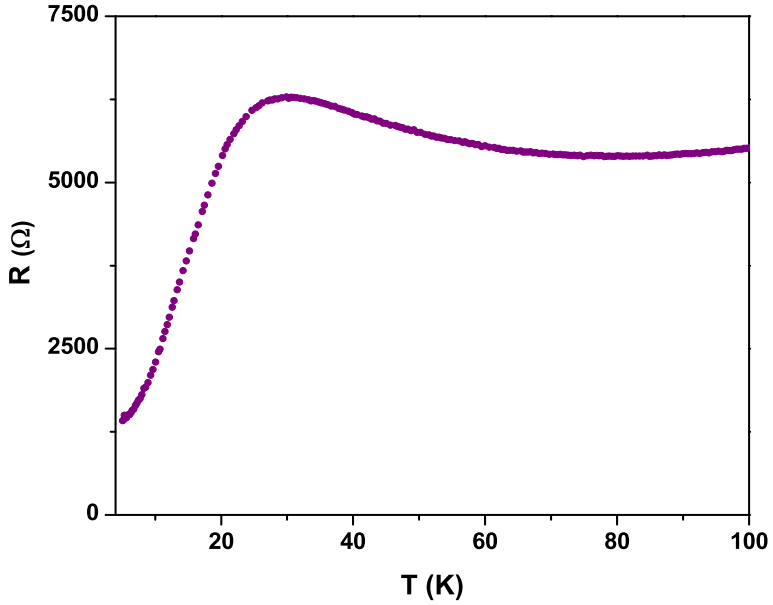

Figure 3.1: Temperature dependence of resistance in a 170 nm-wide nanowire fabricated out of an underdoped LSCO film. The resistive transition is incomplete, showing a high residual resistance, larger than 1 kΩ.

The sudden drop in measurement R(T)typically occurred at essentially the same T_c as the value measured by mutual inductance technique in the same film before it was patterned. In nanowires patterned out of underdoped LSCO films with the nominal doping level $x = 0.11$ and $x = 0.10$, we measured abrupt resistance drops at 19 K, comparable to the bulk value of T_c. An obvious problem

that arose for this fabrication process, as observed by electrical transport measurements, was the presence of residual resistance in R(T) curves even at T= 4 K, as seen in Fig.3.1. Consistent with this finding was the absence of critical current in the I-V characteristics. Such incomplete resistive superconducting transitions were observed in the majority of devices measured. Residual resistance values varied from 10 mΩ to 10 kΩ, while our resistance measurement resolution was better than 1 mΩ. Lower residual resistance values were generally found in wider, optimally doped, Au-capped LSCO nanowire devices, while higher residual values were typically seen in narrower, underdoped, bare nanowire devices.

In principle, incomplete superconducting resistive transitions could arise intrinsically as a result of phase-slip processes. These phase slip processes broaden the resistive transitions and fit an exponential R(T) dependence expected from the widely accepted Langer-Ambegaokar-McCumber-Halperin (LAMH) theory of thermally activated phase slips (TAPS). However, we rule out this explanation, because the nanowires were up to two-orders-of-magnitude wider than the coherence length - the scale were such behavior is usually observed [41,42].

Device #	1	2	3	4	5	6	7	8	9	10	11	12
Width (nm)	80	80	140	140	180	200	200	200	200	250	300	300
R (Ω/□)	156	556	OL	OL	3.4	7	15	120	350	1.8	2.7	2.7
SEM exposed	Yes	Yes	Yes	Yes	No	Yes	No	No	Yes	No	No	No

Figure 3.2: The effect on the residual resistance of a nanowire exposed to a 5 kV SEM electron beam. OL = overload, i.e., resistance $>$ 1 GΩ. For best comparison, all the measured devices fabricated from the same LSCO film are listed here.

We surmise that the primary cause of the residual resistance in our nanowire devices are extrinsic factors such as electron-beam damage, ion-beam damage during Ar^+ ion milling, or both. Electron irradiation was previously observed to introduce defects in cuprates [43], so electron beam-induced defects may be a likely culprit. In Fig.3.2, we compare the values of residual resistance in several bare LSCO nanowire devices that were exposed to an electron beam during SEM characterization, along

with others that were not exposed. For sure, there is noticeable damage caused by charged beams interacting with our samples, in this case the low-kV electron beam from the SEM. This also brings to the fore, possible damaging effects which may be caused by the charged Ar^+ beam interacting with our sample in the pattern transfer fabrication step.

Because studies of the intrinsic physical properties of cuprate nanowires relies on fabricating pristine nanostructure, devices showing incomplete resistive transitions cause interpretation of data to be most difficult. To further highlight why developing robust nanowire fabrication technology was pursued, we describe preliminary results from a telegraph noise transport experiment on nanowires in the next section.

3.3 Stripes and Telegraph Noise: A Motivation for Nanowire Fabrication

When the parent Mott insulator compound in the cuprates is doped with holes, interesting nanoscale electronic phases form[16] in which charge and spin are modulated atop the host lattice. One particular important electronic phase that has garnered much interest is that of the stripe and nematic phases[13,15] in which the charge carriers form one dimensional rivers of charge separated by antiferromagnetic order in the intervening domains. Pinned my disorder, according to a Random Field Ising model proposed, these objects can form so-called nematic domains which are aligned along either crystal axis direction in the a-b plane of the cuprate[44], with the particular orientation of any one patch controlled by the local disorder. Fig.3.3 shows an artistic rendering of these quilt like nematic orders align along the orthogonal crystal axis directions. Neutron scattering[45] has found indications of this charge and spin order and pegs the length scale for the stripe correlation length to be between 35-40 nm for YBCO[46]. Theoretical proposals for the detection of these domains have appealed to the resistance anisotropy which can be measured[47]. In particular their fluctuations from one domain direction to another would give rise to a two-level switching or telegraph noise signal, in the simplified case[44] which

are also predicted to exhibit magnetic hysteresis. To be sensitive to such fluctuations, because of the purported sizes of the domains, one would be most sensitive were the measurement confined to nanostructures. Otherwise there might be ensemble averaging of the purported two-state switching.

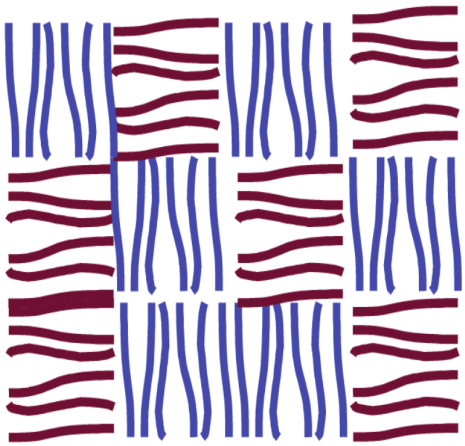

Figure 3.3: A cartoon configuration of nematic domains. These domains align along crystal axes and are pinned by local disorder. When they fluctuate from one orthogonal direction to another, it gives rise to resistance fluctuations from the anisotropy. Reproduced from [44]

An experiment to monitor resistance changes over time was carried out in the YBCO crystal system fashioned into single nanowires [22]. Resistance fluctuations of 0.1% was observed in a temperature range between T_c and T*, coinciding with the temperature range in which the pseudogap is prominent (Fig.3.4). As such, this is highly suggestive of transport measurements having access to this interesting electronic phases in the time domain. A follow-up experiment [39], still in YBCO, found anomalous excess spectral noise in the underdoped regime with amplitudes tracking the critical temperature (mapped back to doping) in their oxygen doped material.

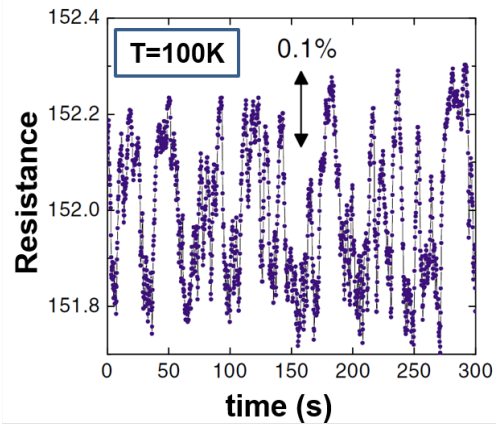

Figure 3.4: Resistance fluctuations on the order 0.1% seen in YBCO nanowires of widths comparable to 100 nm explained by a fluctuating nematic domain model. The nanowire size, by the estimates of[46] would fit about 2 domains making it more sensitive to individual fluctuators. Adapted from[22]

3.4 Measurement in LSCO: The Noise is the Signal

The observation of telegraph noise signals in YBCO begs the following question: Is the observed telegraph signal universal to all cuprates or specific to YBCO ? There is also the question of whether the noise arises singly from the copper oxygen planes in the unit cell or possibly from the copper oxygen chains. In LSCO, with its single copper oxygen plane and no chains, it would be ideal test bed for such questions in which the data can be interpreted in a more straightforward fashion. Other questions of interest relate to finding out the temperature dependence of these noise signals, should they be present in LSCO, on doping and length scales. Is it true that the noise signals, again if present, would only be observable in the pseudogap regime of the compound. The current leading thinking is that nematicity occurs in a subset of the pseudogap phase; that is, the pseudogap phase enables nematicity, but it's not equal to nematicity[19]. Accessing pseudogap physics in this way would provide a fresh lens through which to view the cumbersome and entangled relationship this pseudogap state has with superconductivity. With such important questions to answer, we carried out time domain measurements in

LSCO nanobridges patterned with the recipe outlined in chapter 2.

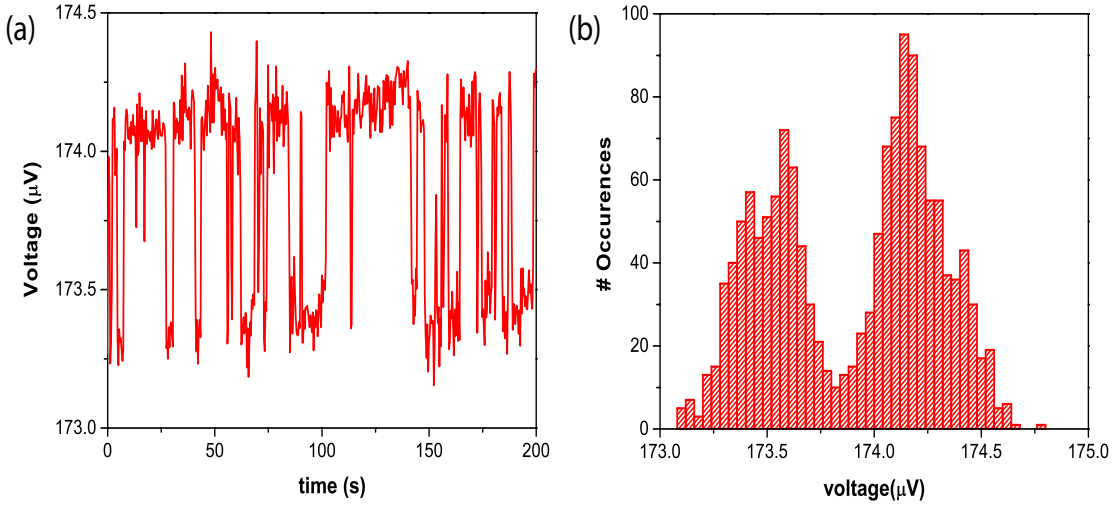

Figure 3.5: (a) Voltage versus time measurement of a single underdoped bridge in the normal state. T_c = 19 K for the bulk film, and the measurement temperature here is T = 41 K. T* estimated to be 150 K for this particular doping of x = 0.10. Bridge width, w = 170 nm and film thickness is 26.4 nm. Voltage drop measured across 500 nm of the long nanowire. (b) Shows a bimodal histogram of the two-level telegraph switching shown in (a).

We carried out a DC noise measurement by applying constant current bias and monitoring the voltage over time as shown in Fig.3.5. Telegraph noise signals were observed with clear and distinct bimodal distribution of voltage values. The film thickness was 26.4 nm (40 ML) and the bridge width was sub-200 nm. From estimates of the T* = 150 K for this doping of x = 0.10, and the measurement temperature for this result of T = 41 K, we are in the pseudogap regime. While we have observed the telegraph signal, we are uncertain about the true origin. The device in Fig.3.5 displays an incomplete superconducting transition much like in Fig.3.1 but with a higher residual resistance of 7.5 kΩ. To probe the true and intrinsic nature of the domains, we need to start with a nanowire that displays complete superconductivity with a transition into a true Meissner, zero resistance state. Carrying out telegraph noise measurements then, in the normal state, would be insightful.

The remainder of the thesis was devoted to creating pristine nanostructures to accomplish inter-

esting experiments probing the native electronic phase of the materials. To do this, I began a system assessment of each part of the lithographic process to pinpoint the culprit. In this thesis, I will be summarizing this long and arduous task.

3.5 The Importance of Ion Milling

In the next several sections, I will be focusing on the study of the effects of ion milling on the nano-lithographic process. However, we have not completely ruled out damage that may come about from exposure to electron beams during the e-beam write process itself. With this in mind, we proceed with discussing experiments focused solely on ion milling and how it has impacted the quality and minimum widths of nanowires we have been able to fabricate.

3.5.1 Results: 1.27 mA/cm^2 Beam Current Density Milling

With the need for more refined fabrication ever more necessary, we modified the ion-milling step to be less invasive. We scaled the beam voltage down from 500 V - 1 kV to 350 V, and the beam current from 50 mA down to 25 mA, the minimal value for sustaining the Ar^+ plasma in our system. The beam current settings used amount to a beam current density of 1.27 mA/cm^2 - an important parameter. In addition, during the ion-milling process, we cooled the sample holder by liquid nitrogen, in order to minimize possible oxygen loss from the LSCO film. For the optimally doped LSCO films with reduced beam voltage and beam current during ion milling, we observed an improvement in the nanowire device properties (Fig.3.6).

In Fig.3.6, we show LSCO devices with complete superconductor resistive transitions observed in Au-capped nanowires of varying widths as indicated, fabricated on the sample LSCO film. Of the data shown in Fig.3.6, the narrower wires show overall higher resistance values, with the exception of the wires of width 450 nm and 500 nm where we suspect a local substrate defect or scratch could

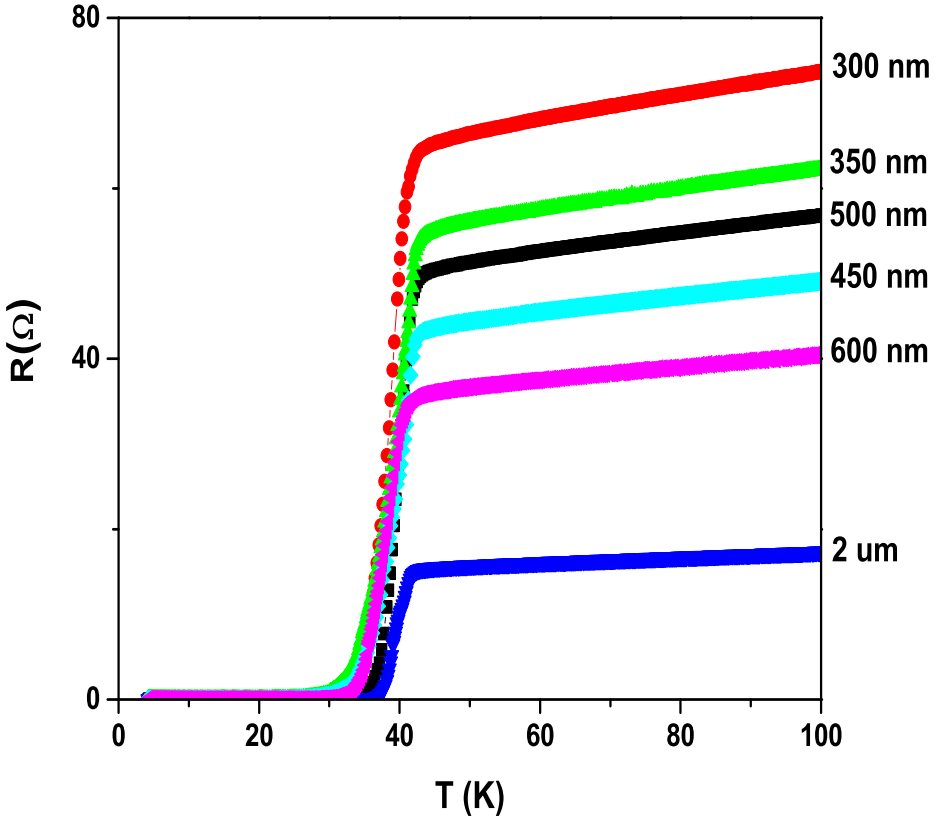

Figure 3.6: R(T) characteristic of six devices of varying widths, all fabricated on the same optimally-doped LSCO film for easier comparison. The pattern transfer was carried out using a reduced beam voltage (350 V) and current (25 mA) during the ion milling step. Every measured device fabricated from the same LSCO film shows a complete superconducting transition down to 300 nm widths. The resistance was measured with a current bias of 1 μA.

have given rise to a higher resistance in the 500 nm device. We have also measured the corresponding values of critical current density for the same set of LSCO devices, between $j_c = 10^7$ - 10^8 A/cm^2. Such high critical current density values for Au-capped nanowire devices with complete superconducting transitions indicate how crucial the ion-milling step can be in patterning nanowire devices in cuprates, particularly in LSCO. With all the listed precautions to mitigate the damage from the ion milling process with the ion milling beam current of 25 mA, we were able to fabricate nanowire 4-terminal devices down to 300 nm, with complete superconducting transitions. The role of the ion-milling step has been suggested by other groups working with YBCO films[25].

3.5.2 Low Beam Density Milling

3.5.3 Results: 0.4 *m*A/cm^2 Beam Current Density Milling

With the narrowest nanowire structure of width 300 nm for optimal doping, obtained with a beam current of 25 mA and 1.27 mA/cm^2 beam current density we sought further improvements to the process by further refining the ion milling step. We had successful diagnosed this as the impediment to obtaining narrower structures still. For underdoped samples more care needed to be taking in their fabrication as they are more prone to damage. For this section we collaborated with the Tafuri group in Naples, Italy and Dr. Davide Massarotti, who performed the ion milling in Naples. The ion milling system could sustain a stable plasma at 5 mA over 4 cm diameter which corresponds to a beam current density of 0.4 mA/cm^2, a decrease by a factor 3 from the previous beam densities used for etching.

I will discuss a systematic experiment designed to tease out what happens when the beam current density used for nanowire fabrication is in the sub-1 mA/cm^2 range. In addition, we perform this test on three electron beam patterned samples with one optimally doped (named OPT for the remainder of the discussion), a second underdoped (UD) and finally a bilayer sample (BI) of 10M and 10I sustaining interface superconductivity with optimal doping. The lithography procedure used is as outlined

in chapter 2. Each sample consisted of 20 LSCO bridges ranging in widths from 130 nm to 10 μm pattern into 2 columns of 10 devices each. In total 60 single bridge devices were characterized for this study. The device labels and their respective widths are given in Table.3.1.

Patterned Nanobridge Widths		
Device number	Column A nominal width	Column B nominal width
1	1 μm	400 nm
2	500 nm	300 nm
3	1.5 μm	350 nm
4	2 μm	200 nm
5	10 μm	450 nm
6	5 μm	600 nm
7	6 μm	700 nm
8	3.5 μm	400 nm
9	3 μm	200 nm
10	4 μm	130 nm

Table 3.1: Sample was patterned in two columns of 10 devices each. Above, we have tabulated the design widths for each corresponding bridge and device number.

Here is a summary of the sample compositions:

M: Metallic (LSCO $x = 0.44$) ML: Monolayer OP: LSCO $x = 0.16$ I: Insulator (LCO)

1. Sample OPT : 2 ML (M) + 28 ML (OP), Optimally doped.
    - Thickness: 19.8 nm.
2. Sample UD : 2 ML (M) + 20 ML (OP), Underdoped.
    - Thickness: 14.5 nm.
3. Sample OPT : 10 ML (M) + 10 ML (I), Bilayer/Interface superconductivity.
    - Thickness: 13.2 nm.

Two-point, probe station measurements of the sample surfaces were carried out before the ion milling process (Table.3.2). For OPT, a surface resistance of 500 Ω was measured, 50 kΩ for BI, and finally UD registered a 10 kΩ 2-probe surface resistance. Measuring the surface resistance post-ion milling, was used to confirm the termination of the ion mill procedure at the LSAO insulating substrate layer. If the LSCO film has been milled all the way through to the LSAO substrate, then an overload (OL) resistance is measured. If not, a finite resistance is measured and the film is placed in the ion milling chamber again for additional milling. Samples were glued to a copper stage with silver paste for proper thermal anchoring. The samples were subsequently cooled by LN_2 for all Ar^+ milling sessions.

Argon Ion Mill Conditions						
Samples	Thickness (nm)	Initial resistance	Beam voltage (V)	Beam current (mA)	Etch time (min)	Etch rate (nm/min)
Sample OPT	19.8	500 Ω	305	5	8	2.5
Sample UD	14.5	10 kΩ	305	5	6	2.4
Sample BI	13.2	50 kΩ	305	5	7	1.9

Table 3.2: Argon ion milling explicitly tabulated for each of the samples. Beam voltage was not a parameter that was varied. A voltage sufficient to provide sufficient sputter yield in milling was used.

Both samples OPT and BI were ion milled in two steps. BI was first ion milled for 3 minutes, and then 4 minutes for a total milling time of 7 minutes. OPT was first ion milled for 4 minutes and then again for 4 minutes the second round for a total milling time of 8 minutes. The two step milling was used since in this first iteration it was unclear how long to mill the sample. In between the ion mill etch steps, the sample surface resistance was measured in a 2-point probe station. UD was milled in one session for a total time of 6 minutes. The milling parameters are summarized in the table (Table. 3.2). Of course, the etch rates given are lower bounds since the time was not optimized so that the etching process terminated just at the insulating substrate layer.

Measured resistance versus temperature curves are shown for the ion milled bilayer sample in Fig.3.7 and a corresponding table showing resistances for particular devices is outlined in Table.3.3.

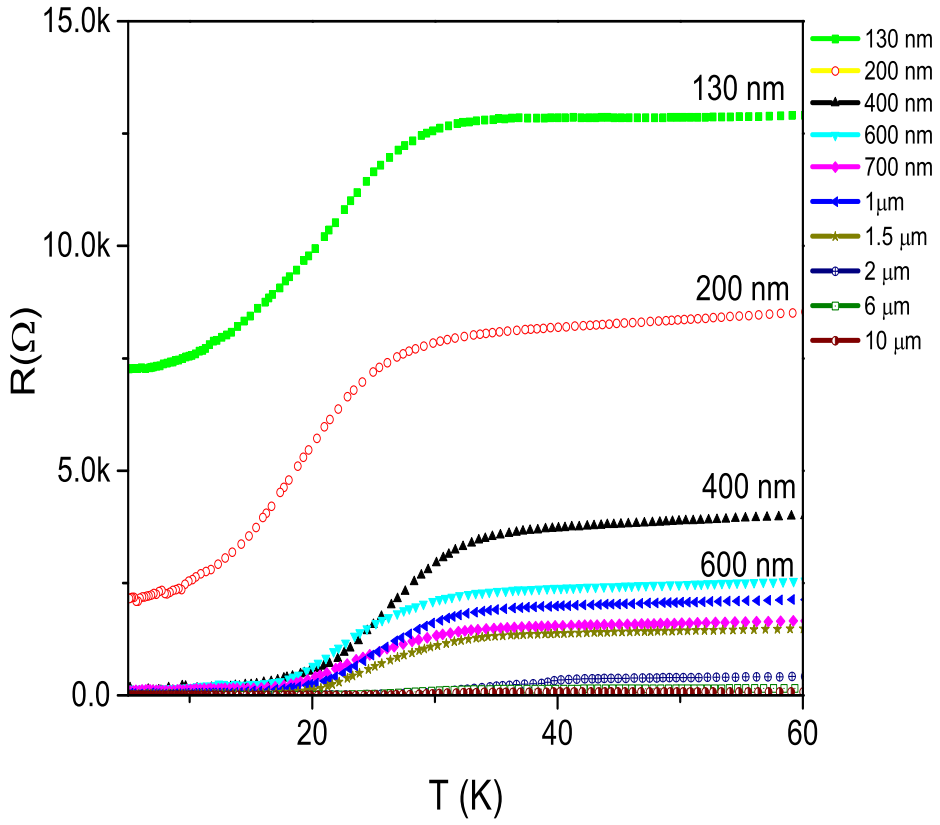

Figure 3.7: Resistance vs. temperature plots of several devices measured on the bilayer sample, BI sustaining interface superconductivity. For narrow bridge widths, we observe an incomplete superconductivity transition. Narrow bridges were current-biased with low current (100 nA) to minimize any adverse effects for using high bias currents. Microbridges ($\geq 1\mu$m) were biased with 1-2 μA currents.Bridges of widths 130 nm and 200 nm have greater than 2 kΩ resistances at T = 4.2 K. Four narrowest nanowire curves are explicitly highlighted for easier comparison.

Table.3.4 shows the critical bridge width for the underdoped samples. A critical bridge width is defined such that devices with larger widths are completely superconducting and those which are narrower display incomplete superconducting transitions and finite residual resistances. That width, is roughly 400 nm for the underdoped sample.

Residual resistance values at T = 4 K for Bilayer Nanobridges		
Nanowire Nominal Width	Residual Resistance (T = 4 K)	Device Number
130 nm	7.2 kΩ	10B
200 nm	2.16 kΩ	9B
400 nm	100 Ω	1B
600 nm	116 Ω	6B
700 nm	105 Ω	7B
1 μm	23 Ω	1A
1.5 μm	15 Ω	3A
2 μm	0 Ω	4A
6 μm	0 Ω	7A
10 μm	0 Ω	5A

Table 3.3: Tabulated values of the measured residual resistance at T = 4.2 K for the characterized bilayer bridges. The narrower the device width, the greater the residual resistance observed, indicating extrinsic damage from the lithographic process as the bridge linewidth decreases. At a nominal 200 nm width, the residual resistance drops drastically from 2.16 kΩ to 100s Ω. This piece of data may indicate the characteristic fall off length scale of the lateral straggle or damaged region. The minimal bridge width found to be superconducting was 2μm

This is an improvement over the 25 mA ion beam parameter which had a critical width of greater than 1 μm. On the underdoped sample, there are two devices patterned with similar design widths of 400 nm. One shows a finite resistance at T = 4.2 K, while the other exhibits complete superconductivity. This may be due to a local material defect during the lithographic process. The observations of different critical widths from this experiment along with previous experiments patterning underdoped sample suggests their extreme sensitivity requires greater care in the fabrication process. Still, the bilayer samples are even more delicate to pattern as the critical width is larger still, 2μm compared to the observed 400 nm for underdoped sample. Further refinement of our lithographic process will be needed to achieve superconducting nanowires with narrower widths for underdoped and optimally doped samples. In carrying out current voltage measurements as shown in Fig.3.8 for the underdoped 130 nm wide bridge, we found remnants of superconductivity in the bridge. Although this bridge displayed an incomplete transition with a 9 Ω resistance at 4 K, its I-V was non-linear and s-shaped at

Residual resistance values at T = 4 K for Underdoped Nanobridges		
UD Device number	Residual Resistance (T = 4 K)	Device Number
130 nm, run1	9 Ω	10B
130 nm, run2	19.5 Ω	10B
130 nm, run3	23 Ω	10B
200 nm	105.2 Ω	4B
200 nm	14 Ω	9B
300 nm, run1	130 mΩ	2B
300 nm, run2	1.5 Ω	2B
350 nm	7.5 Ω	3B
400 nm	1.2 Ω	1B
400 nm	0 Ω	8B
600 nm	0 Ω	6B
700 nm	0 Ω	7B
1 μm	0 Ω	1A
2 μm	0 Ω	4A

Table 3.4: Extracted non-zero residual resistance values. For the 130 nm nanobridge, multiple measurements were carried out for characterization. We observed an aging effect. Different and ever increasing values of the residual resistance were measured through multiple runs. A similar effect was seen for the 300 nm bridge, with an increased residual resistance of up to an order of magnitude observed. Both devices showed aging effects.

relatively low voltage values less than 2.5 mV. A critical current of less than 20 μA could be observed. Another indication of the improvement of the recipe, but yet another indictment on the destructive effects of high beam current milling parameters.

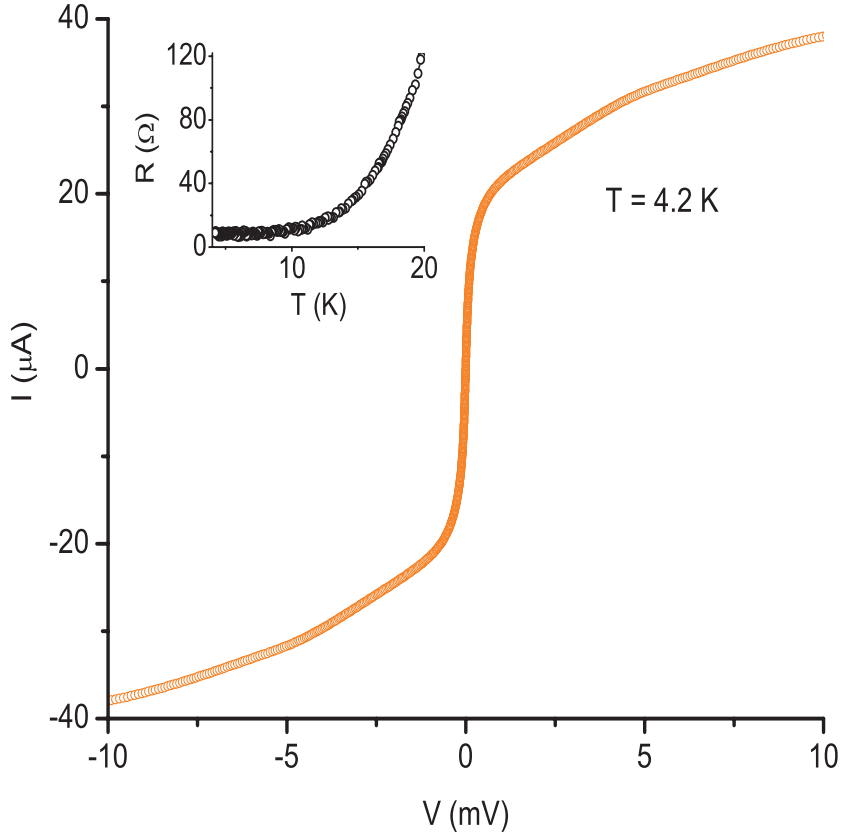

Figure 3.8: Current-voltage measurement for a 14.5 nm thick LSCO underdoped nanowire 130 nm wide with doping x=0.11. This I-V shows non-linear behavior reminiscent of a completely superconducting device. The inset shows resistance versus temperature zoom for the same device showing a residual resistance of 9 Ω. The RT curve in the inset was measured with 100nA bias.

For the optimally doped sample, OPT, all measured devices showed complete superconducting transitions. We will focus specifically on the narrowest of these. Both 200 nm nanowires (4B and 9B) displayed zero residual resistance as did the narrowest wire of width 130 nm for this milling recipe performed with beam current density of 0.4 mA/cm^2 and beam current of 5 Ma. This is a marked

improvement over the ion milling process that used a higher beam current (25 mA) and beam current density of 1.27 mA/cm^2. The 25 mA and 1.27 mA/cm^2 milling recipe had a process critical width of 300 nm while the 5 mA and 0.4 mA/cm^2 recipe has critical width of at most 130 nm. This strongly indicates that the crucial tuning parameter to achieving narrower nanostructures is a reduced ion milling beam current and beam current density. The most success has been achieved with the optimally doped bridges which in some sense are more robust to the extrinsic damage resulting from the lithographic process.

3.5.4 Results Summary

In decreasing the beam current from 25 mA over a 5 cm source down to 5 mA over a 4 cm source, we greatly improved the achievable narrow nanowire width for optimally doped samples to at least 130 nm. For the underdoped sample we were able to measure nanowires of widths at least 400 nm that were superconducting. However, not all devices with 400 nm design widths showed superconductivity. Nevertheless, this showed drastic improvement over previous procedures carried out at 25 mA beam current. Another empirical improvement even for those nanowires that showed incomplete transitions was the decrease in residual resistance values by at least 3 orders of magnitude. The bilayer sample was the most sensitive to the process still, with an achieved minimum width of a superconducting device 1.5 μm. However, the question remains of what plays a more important role in fabricating superconducting nanowires: is it the beam current magnitude at the source ? or is it the beam current density of the source ?.

3.6 Achieving Superconducting Sub-100 nm Narrow Nanowires

3.6.1 Results: 0.03 - 0.06 mA/cm^2 Beam Current Density Milling

In this section we report further improvement on our previously outlined fabrication recipe and have identified the critical factors in the lithographic process that have led to patterning sub-100 nm optimally doped and bilayer LSCO bridges. MBE films in this study had thicknesses of 30 ML (19.8 nm) and 20 ML (13.2 nm). Two groups of films were patterned: LSCO films at optimal doping, $x = 0.16$ and bilayer with 10M + 10I composition with interface superconductivity. In particular, these bilayer samples have been shown to be quite sensitive to extrinsic damages arising during the lithographic processing. The narrowest critical bridge width achieved for the bilayer samples was 2 μm. To test this trend of decreasing beam currents and milder dry etching yielding narrower superconducting devices, we utilized an ion milling source at the Chalmers University MC2 cleanroom facility (Fig.3.9) with beam current magnitudes of 5 mA and 10 mA over a 15 cm source.

This corresponds to beam current densities of 0.03 - 0.06 mA/cm^2, close to an order of magnitude lower than in the previous experiment with the 5 mA beam over a 4 cm source. At these low beam currents and densities, etch times of up to 45 minutes were needed to etch down to the substrate. LN_2 stage cooling was used as a continuation of lessons learned so as not to change many variables at once. The samples were mounted on the top face of a hollow steel rod which was cooled by LN_2. Rotation was performed during ion milling about the beam axis with a low power motor wheel connected to the steel rod. Rotation was used to ensure even etching of the sample. Without sample rotation, there can be re-deposition of the sputtered material along the walls of the etched pattern.

Ar^+ beam currents between 5 mA - 10mA and beam voltage 300-315 V were used. For the samples in this study, we used a SIMS end point detector during the ion milling process to help determine when the film was etched completely, and down to the substrate. Such a technique allows the prevention of over-etching the delicate nanostructures. We found this to be a crucial tool in gaining better

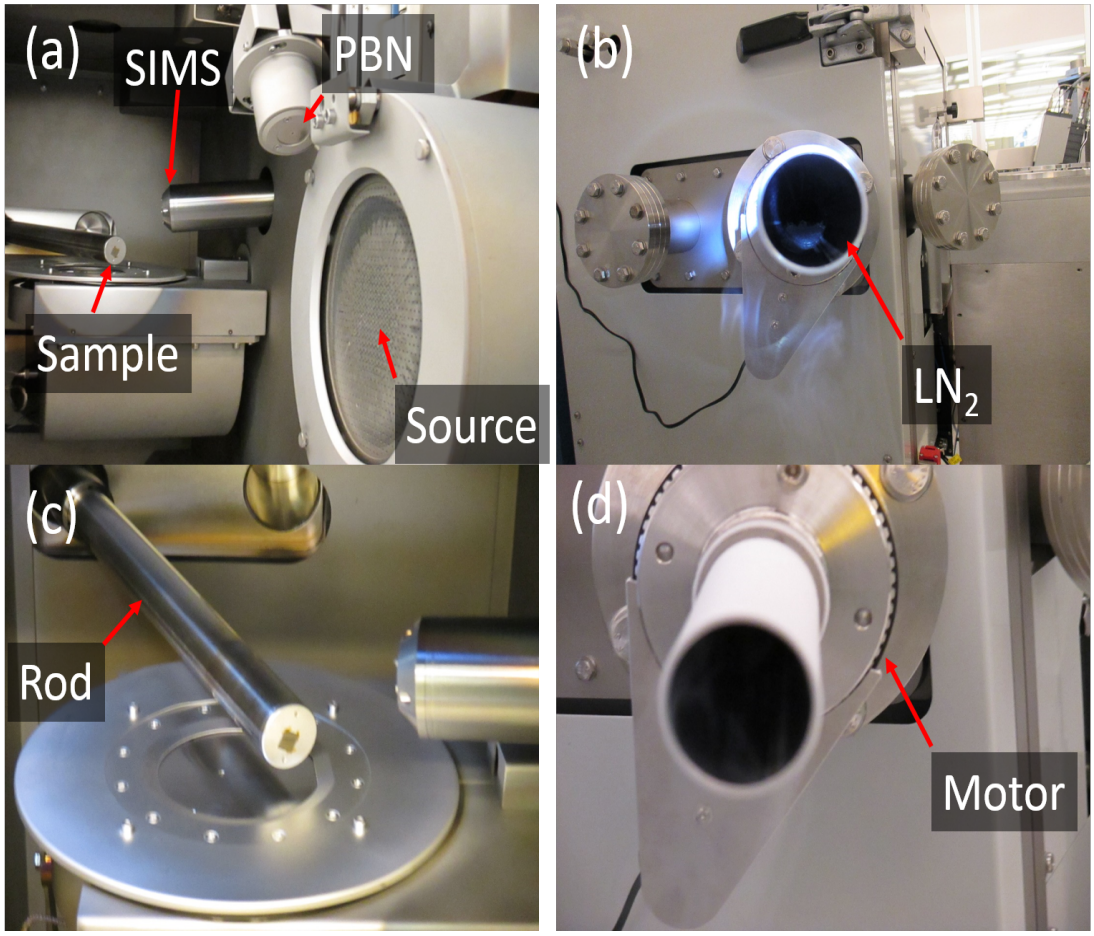

Figure 3.9: (a) The Chalmers milling system adapted from an Oxford Ion Beam Etching tool innards showing a source of 15 cm diameter, a plasma bridge neutralizer (PBN), SIMS endpoint detection close to the sample mounted on the top face of a hollow rod. (b) Back side of the rod hollow for LN_2 loading.(c) Close up of road with sample mount and the SIMS detector jutting from the right. (d) The rod is frosted after LN_2 poured in to cool down the sample.

control of the dry etching patterning step. Post Ar^+ ion milling, the electron beam resist mask remains and can either be removed by dissolution in a remover solvent or by a terse oxygen plasma reactive ion etch (RIE). The final structure is the four probe nanowire pattern in the cuprate film for four-point electrical characterization measurements. Multiple devices were patterned on each cuprate film. We patterned an array of nanobridges. Fig. 3.10 shows scanning electron microscope images of the completed devices. The narrowest width achieved by this technique is seen to be 80 nm.

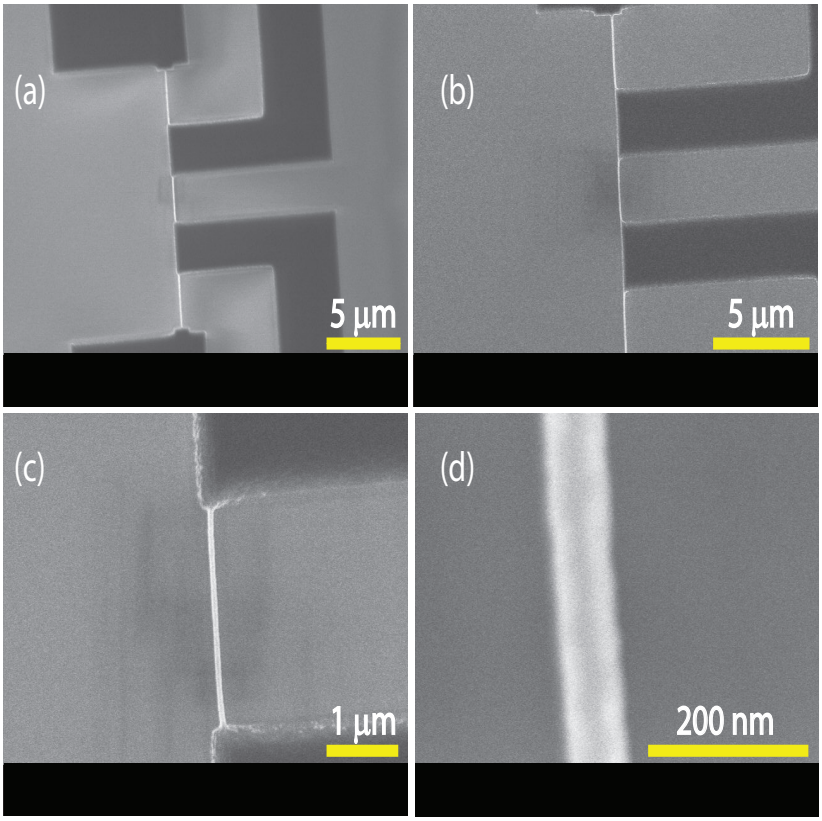

Figure 3.10: A scanning electron microscope of 2 different devices (a) and (b) both the same width, 80 nm. The patterned is optimally doped and 19.8 nm thick (c) shows voltage drop of device in panel (a) measured across 2.5 μm, taken to be the effective nanowire length. (d) Zoom-in of device (a) showing sub-100 nm nanowire width.

Previous electron beam lithographic techniques have used either titanium or carbon as etch masks,

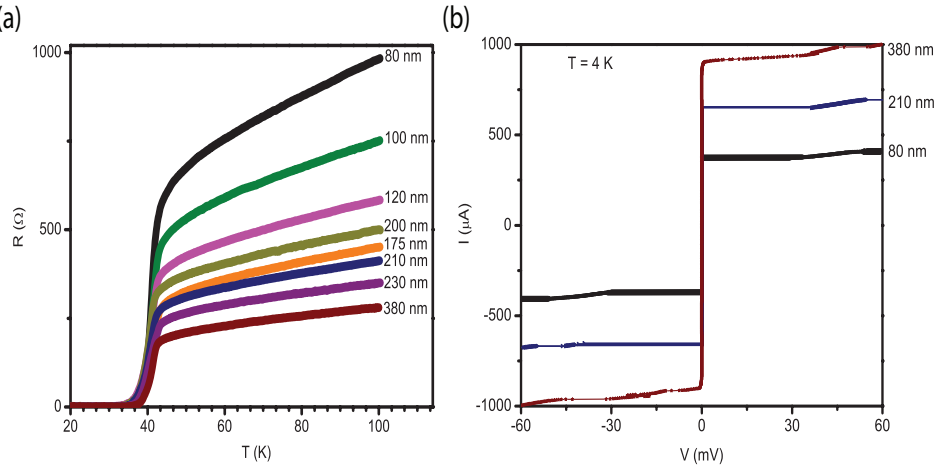

Figure 3.11: (a) Resistance versus temperature measurements for nanowires in the mesoscopic regime show comparable critical temperatures across different widths. For easier comparison,all devices shown here were patterned on the same optimally doped film with a thickness of 19.8 nm. A 100nA bias current was used. (b) Current versus voltage plot of some of the devices shown in (a) spanning wide range in bridge width, measured at T = 4 K.

rather than the negative toned resist mask utilized here as explained in chapter 2. For the titanium hard masks, a dip in diluted HF solution is needed to remove the metal atop the cuprate film which may be destructive to the film. Additional processing steps are needed for the carbon mask method. Nevertheless, sub-200 nm nanobridge widths have been achieved using either procedure. Our fabrication recipe has the advantage of being more streamlined as it does not require a lift-off step. Current biased electrical transport measurements were carried out in a four-probe configuration to characterize the patterned devices. Resistance versus temperature measurements shown in Fig.3.11a were performed to pinpoint the critical temperature for the nanobridges. Current-voltage measurements to observe the critical current in Fig.3.11b were also conducted. Current-voltage measurements as a function of temperature are also possible in this configuration. Bias current values for resistance versus temperature measurements used in the study ranged from 10 nA - 1 μA. Typically we used a current bias value of 100 nA ensuring we were in the linear bias regime, thus avoiding any non-linearities arising from

high current biases. The current-voltage scans performed at the cryostat base temperature of 4.2 K, used in these experiments, corroborated the linear current bias hypothesis for each of the measured devices. The superconducting devices had base temperature critical currents much higher than the bias currents used for resistance characterization. Electrical transport characterization of LSCO nanowire devices was carried out using a home-made variable temperature (4 K to 300 K) cryostat, using a low noise four-terminal configuration method. Resistance versus temperature, R(T), and current-voltage (I-V) characteristics were measured for the fabricated nanowire devices using a DC current-bias technique. I-V measurements were used to measure I_c for superconducting nanowires below the superconducting transition temperature. Low-current bias conditions, below the device Ic, were used for R(T) measurements. The critical temperatures measured for the nanobridges devices patterned from an optimally doped LSCO film (Fig.3a) were close to the bulk film value. Bulk critical temperatures in our films were measured using a non-contact mutual inductance technique. The milling procedure with 0.03 - 0.06 mA/cm^2, shows a high yield for devices that were superconducting after fabrication. All the devices measured for the optimally doped samples patterned showed complete superconducting transitions. The narrowest nanowire has a normal state resistance higher than the wider bridges. Correspondingly, the widest bridge has a lower normal state resistance and we observe a slightly higher critical temperature in the resistance measurement. A similar pattern is seen for all the nanowires except for the nanobridge with 175 nm width which deviates from this scaling. This may be due to a local extrinsic film defect. Critical currents in Fig.3.11 in the upwards of 300 μA but below 1 mA were observed for the nanobridges measured. Critical current densities observed for these optimally doped nanowires were in the range of 10^6 - 10^7 A/cm^2. These values are an order of magnitude (for our lowest critical current values) less than the depairing critical current in the GL-theory necessary to break up cooper pairs. We speculate we are below this limit for this particular film because it was not capped with a protective Au layer. Other studies have shown the Au cap to influence the critical current values observed. We speculate the ex-situ Au shunt acts to mitigate local charging effects and dissipate

heat from the ion milling process. Higher critical current values an order of magnitude higher than sans Au cap have been reported. In our previous study, we found this trend in our films. In those Au-capped films, we found critical current values in the range, 10^7 - 10^8 A/cm^2, an order of magnitude higher than those in the present study. Also, because of our device geometry with the voltage probe intersecting the long nanowire, current crowding effects become important[26,48,49,50,51].

In summary, in this section we have shown for the first time reported in the literature, single LSCO nanowire devices in the sub-100nm range. We identified crucial steps in the lithographic process, taking particular care during the Argon ion milling etching step: employing both SIMS end point detection for over-etching prevention and a LN_2 cooled sample stage. Our lithographic procedure for achieving these narrow linewidths was streamlined requiring fewer process steps than previous techniques. The narrow linewidths were achievable with high yield for devices showing complete superconducting transitions in optimally doped films. In this study strides were made in opening up pathways for cuprate nanodevice experiments utilizing nanobridges with dopings spanning the entire superconducting dome. Future work will focus on obtaining narrower underdoped structures.

3.7 Ultra-Small Cross-sectional Nanowire

3.7.1 Beam Current versus Beam Current Density

When we patterned a bilayer (10M + 10I) sample with a 5 mA milling current over a 4 cm source, corresponding to a beam current density of 0.4 mA/cm^2, we found the critical width to be 2 μm. In this new experiment, we pursue patterning these highly sensitive bilayer samples afresh with the low beam density ion mill in Fig.3.9. For this study we use a beam current magnitude of 5 mA for milling step, with a lower beam current density of 0.03 mA/cm^2 since the current source diameter is now 15 cm instead of 4 cm. An order of magnitude lower! We tested yet again, what parameter is most important in the nanopatterning process during ion milling. Both processes use the same sample thickness and

composition and the same beam current magnitude but a different source diameter. The significance of this, to hammer on the point further, is that the magnitude of the beam current density is essentially the integrated total current at our sample since our chip is 1 cm^2.

SIMS monitoring during ion beam etching of the bilayer sample was pivotal in determining the stop time of the etch. Due to the SIMS sensitivity, we were able to see the bilayer sample etched layer by layer by monitoring both the strontium and aluminum channels. This is shown in 3.12. Determining when to stop the mill so as not to over-etch the sample is key.

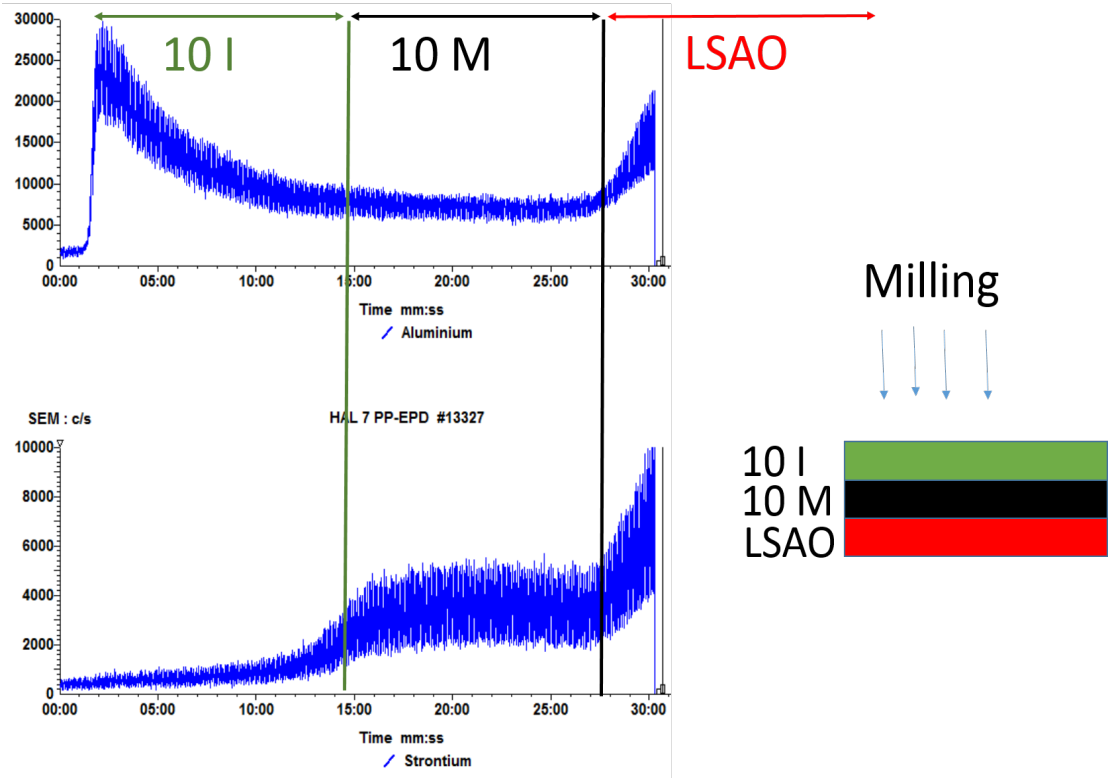

Figure 3.12: An annotated SIMS graph showing the etching of the bilayer 10M + 10 I structure. Aluminum (top graph) and strontium (bottom graph) channels were monitored during etching. Since the metallic layer is more strontium rich, the strontium signal increases at the interface of the bilayer while the aluminum signal remains the same. Once the mill reaches the substrate, the aluminum signal rises.

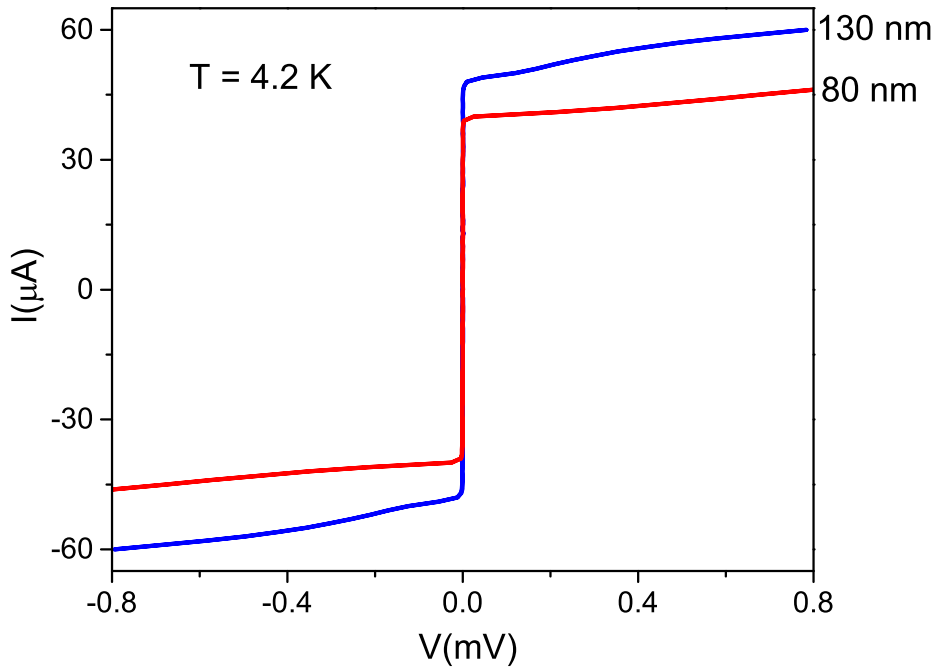

Figure 3.13: The current-voltage characteristics of two bilayer 10M + 10I bridges of widths 80 nm and 130 nm at T = 4.2 K sustaining interface superconductivity. We measured critical currents of 47.4 μA and 39 μA using a 5 μV criterion for 130- and 80 nm wide nanowires, respectively. These amount to critical currents approaching some intrinsic depairing limit.

For this sample, we were able to make a sub-100 nm nanowire of width 80 nm. Another device of width 130 nm was also measured. Both devices were found to be superconducting and therefore sustaining interface superconductivity at these dimensions. The interface thickness is taken to be 0.66 nm. To emphasize, the nanowires made have the following cross-section: 80 $\times$ 0.66 nm^2 (53 nm^2) and 130 $\times$ 0.66 nm^2 (85.8 nm^2). This is the smallest cross-sectional cuprate nanowire reported to date, to our knowledge. Another group has also reported narrow cross-section single nanowires[26]. Their cross-sectional area amounts to 50 $\times$ 50 nm^2 (2500 nm^2), a factor of 50 larger than our narrowest cross-section. Our work in this area holds great promise and further study will be pursued to push

the cross-sectional area even lower. At such small cross-sections, the nanowire cannot sustain vortices, being too small compared to the Pearl length.

We measured the current-voltage characteristics for both devices (Fig.3.13) and observed critical currents of 47.4 μA (130 nm) and 39 μA (80 nm) at the base temperature (T = 4.2 K) of this cryostat. This yielded critical currents of 5.5×10^7 A/cm^2 and 7.4×10^7 A/cm^2 for the 130 nm and 80 nm wide bridges.

3.8 Conclusion

To conclude, we made tremendous strides in our ion milling studies, pinpointing some technical hurdles in fabricating nanostructures across different doping levels of the cuprate. We found the optimally doped non-bilayer samples to be more robust and less sensitive in the strict sense that they repeatedly showed lower critical widths that sustained complete superconducting transitions than their underdoped and bilayer counterparts. For optimally doped LSCO and bilayer films we were able to achieve narrow bridge widths of 80 nm. For the bilayer samples sustaining interface superconductivity, our findings suggest we have obtained critical current densities nearing the depairing limit. Thorough temperature dependent studies of the critical current for these bilayer samples will need to be done. In addition, we found hints that the beam current density may play a crucial role over the beam current value for lower beam current ranges. That is, the net current impinging on the sample matters. More work will need to be done to differentiate between beam current magnitude and beam current density effects and this is because the SIMS detector allowed us to time the endpoint of the etch recipe used for the Chalmers 15-cm diameter source, to avoid over-etching by more than 3 minutes. The recipe with 0.4 mA/cm^2, utilizing a 5 mA beam over a 4 cm source diameter, was not equipped with SIMS.

4

Tunnel Junctions and Nanoconstrictions Patterned by Helium Ion Beam

4.1 Introduction

Some of the results and text of this chapter are from manuscripts in preparation[52,53] titled *Superconductivity in Cuprate Nanoconstriction Devices Patterned by Helium Ion Beam* and also from *Helium*

Ion Beam Patterning of Tunnel Junctions in LSCO Cuprates (Litombe, N.E., Bollinger, A.T., Gozar, A., Huynh, C., He, X., Leng, X., Hoffman, J.E. and Božović, I)

Electron beam lithographic techniques as discussed in the previous chapters rely on using an electron beam to raster across a sample surface spun with resist[21]: either positive or negative tone. This is the well-known technique of electron beam lithography. Ion beams however can be used as part of direct patterning schemes, that is, without an intermediary resist layer. Ejection of the target substrate material giving rise to sputtering or dry etching as well as implantation of the incident ions are all possibilities. Ga^+ focused ion beam is a well known and oft used technique in this regard to pattern nanostructures[54]. Direct patterning LSCO with a scanning helium ion beam at the appropriate doses and energies can locally suppress superconductivity where exposed. A recent study has utilized this technique to create YBCO Josephson junctions[55]. In this chapter, we describe, explore and evaluate direct patterning experiments on LSCO cuprate superconductor films with a scanning He^+ ion beam using a Carl Zeiss Orion NanoFab Helium Ion Microscope (in Peabody, MA) with the objective of fabricating various nanodevices: tunnel junctions, nanoconstrictions and highlighting a pathway towards nanowire direct patterning.

4.2 Direct Patterning with a He^+ Ion Microscope

There are several merits of a helium ion beam microscope. Because of the small beam spot size, as minuscule as 0.25nm[56], it may be possible to achieve high resolution features lithographically. At the very least, the beam spot size in a helium ion microscope will not act as a bottle-neck in achieving ultra-narrow features. More crucially, although the beam spot size may be small for the helium ion beam,

the length scale of secondary electron scattering resulting from the helium ion beam interacting may be crucial. These proximity effects play a ubiquitous role in such lithographic schemes. The secondary electron volume is smaller for He ions. In addition to the ultra-high resolution patterning possibility of the helium microscope, it provides high quality sample imaging possibilities resulting in images with unprecedented depth of field about 5-10 better than for a normal SEM[56]. Therefore, devices can not only be nanopatterned but they can also be imaged at ultra-high resolution and quality.

4.2.1 Charging

As with most instrument using charged beams, patterning insulator substrates becomes challenging due to electrostatic charge build-up causing poor imaging conditions in addition to beam deflections resulting in pattern drift. A negatively charged flood gun in the Carl Zeiss Orion and Orion Plus instrument is used as a beam neutralizer for the substrate in order to mitigate the previously mentioned adverse effects of charging and drift both during imaging and patterning writing.

In our experiment, we worked with LSCO cuprate superconductor films grown atop insulator LSAO substrates. Samples were exposed in the helium ion beam after a dry etching process in an Ar^+ ion mill post a electron beam or photolithographic process. As such, everywhere beyond the photolithography defined pattern consisted of bared LSAO insulating substrate. Low helium ion beam currents (compared to mA range for ion milling, 100 pA - 1 nA for e-beam patterning currents, 10 - 1 μA for transport measurement bias currents) were used for the helium pattern writes. Typical values of the emission beam current used ranged between 1 pA to 2.5 pA. Chamber pressures were in the mid 10^{-7} torr range during writes.

While low beam currents and the flood gun (500 V and 2-3 μA) greatly reduced drift from the charging of our LSAO substrate, nonetheless we found it did not entirely eliminate it. Using the flood gun however, made the drift more predictable and systematic and so we could correct the systematic drift while using the flood by offsetting our pattern write location in the opposite directions as the

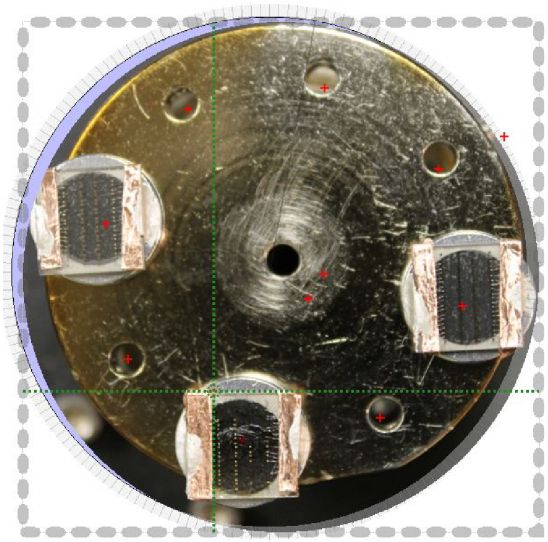

Figure 4.1: Optical image of samples mounted onto chuck in the Orion microscope. Devices were grounded by wirebonding the device contact pads to copper strip shorted to stage mount.

electrostatic drift direction. Without the flood gun, the pattern drift was unpredictable.

To eliminate drift, we proceeded to properly ground our samples in subsequent exposures of other samples. We made a proper grounding path to the Carl Zeiss Orion instrument by first pasting a sticky copper tape on the peripheries of our sample as seen in Fig. 4.1. We then had an exposed copper surface on the top side of the copper tape. Using this conducting top-side we proceeded to wire bond to each of the photolithographically and dry etch-defined contact pads. This provided a conducting path from our micro-bridges of interest to the tape. Grounding the copper tape to the sample chuck which is electrically shorted to the microscope stage using silver paste completed the grounding circuit. When imaged under the helium ion microscope, clear contrast is seen for devices which were grounded properly and those that were not.

In addition, we had no need for the neutralizing flood gun. This is especially useful for materials that are quite sensitive to charge accumulation. Even though the electrostatic drift was eliminated there of course remains the possibility of a long time scale stage/sample drift with respect to the beam

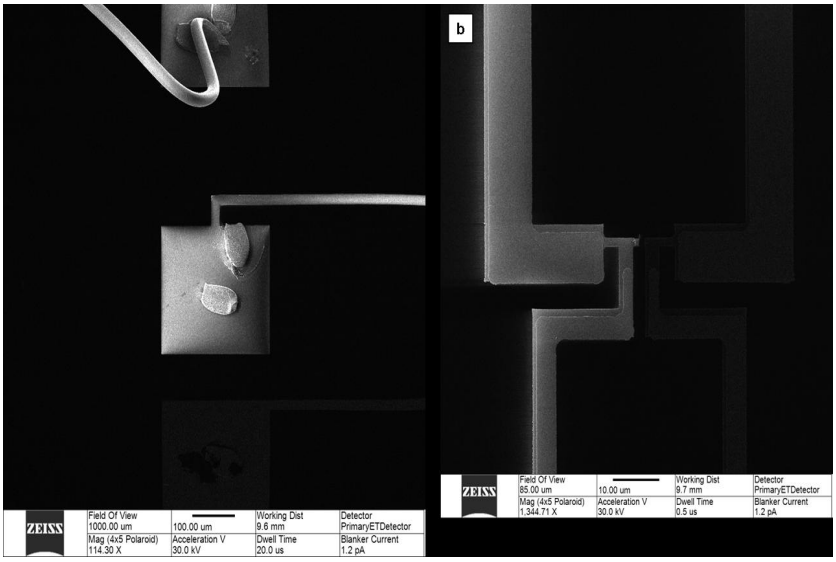

Figure 4.2: (a)Helium ion microscope image of wirebonded contacts pads. The large depth of field can be appreciated. (b) Left half device is grounded to reduce charging while the right half is floated.

which was not be an issue for our quick helium ion beam pattern writes.

The study expounded in the next sections consists of 8 patterned samples, each containing about 20 devices. We discuss those measurements carried out on a subset of these devices.

4.3 Towards Helium Ion Patterned Nanowires

4.3.1 Overview of Method

To create a nanowire using the helium ion writer, we directly pattern two mirror symmetric U-shaped polygons across the LSCO bridge (Fig.4.3, Fig.4.4). Ideally with high enough dose, superconductivity will be suppressed and localized only in the exposed regions while the unexposed regions would remain pristine and maintain their superconductivity. The separation or gap, between these two U-shapes then forms the desired nanowire. The nanowire width is controlled by the separation or gap of the shapes and the length of the horizontal arm of the U-shape controls the nanowire length. The key for

this procedure to work is the essential requirement that the dose needed to suppress superconductivity in the exposed region does not cause lateral straggle while also creating an electrically isolated region. In this experiment, we carried out two schemes: the U-shaped polygon arms (two vertical and one horizontal) could be composed of rectangles or the arms can be written as single lines. We examined both cases in our study.

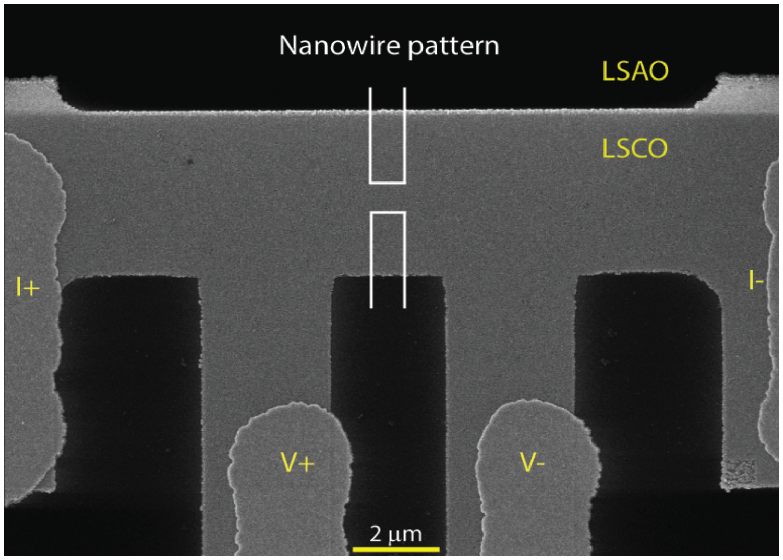

Figure 4.3: Two different devices are show. (a) Helium ion microscope image of a device unexposed by He^{+} beam. The nanowire pattern is drawn in white and consists of two inverted U-shaped polygons. The middle gap or separation defines the nanowire. The length of the nanowire is controlled by the length of the horizontal bar of the U-shaped polygon and the width by the separation between the two.

In this nanowire patterning scheme, particularly for lower doses, it is not necessarily the case that the written pattern completely suppresses superconductivity and creates and isolated structure. Parallel resistance from the vertical arms of the U-shaped pattern must be accounted for. For these micron-sized bridge widths, the larger width of the bridge may win out over the increased resistivity from suppressing superconductivity only along the pattern. To resolve this issue, the rectangular traces of the U-shape may be defined wider but this may cause a pinching effect at the edges of the helium

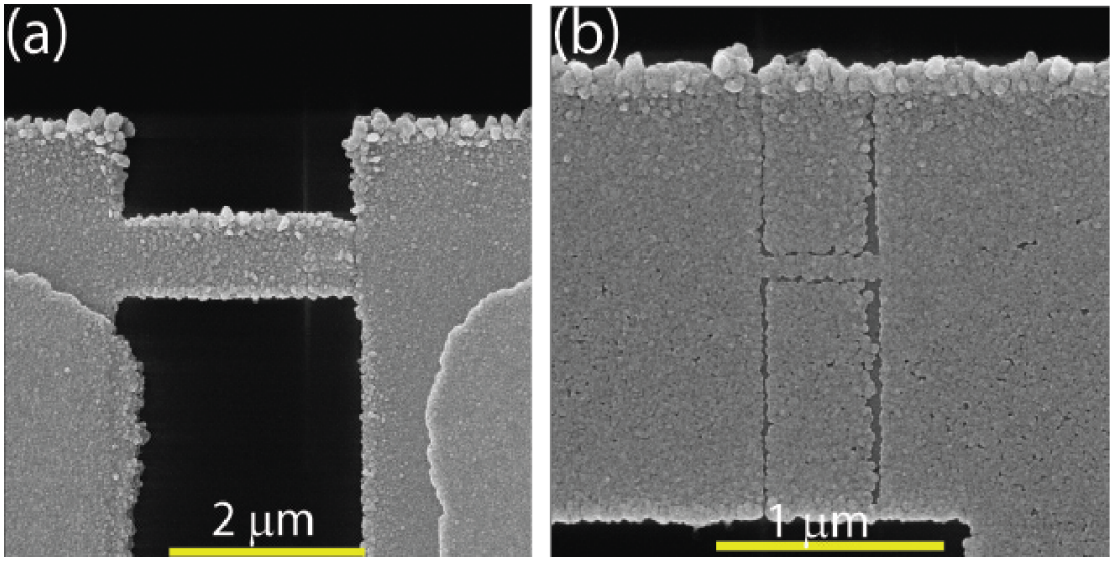

Figure 4.4: (a) Helium ion microscope image of an unpatterned device. Au voltage electrodes flank the left and right of the horizontal bridge. The bilayer sample itself was coated with in situ Au post growth for protection and to mitigate charging during Helium ion writing. (b) At very high doses even the protective Au layer was sputtered and removed in parts of the nanowire pattern traces. Measurements were carried out both before and after Au removal.

beam-defined nanowire pattern. We decided to investigate instead the prospects of using a high dose, single line write to create clean nanowire structures. However, the dose dependent straggle area extent is not known a priori.

4.4 Superconductor-Insulator Transition in LSCO Tunnel Junction Devices

We begin with understanding how single-pass lines across a microbridge affect the cuprate transport properties. Fig.4.5 shows the line pattern. Single line writes were conducted to find out the threshold beam dose where the tunnel barrier is driven from a superconductor with depressed critical temperature, to a metallic regime and finally insulating. The tunnel junctions created by a single-pass line across the microbridge were characterized electrically by resistance versus temperature measurements and current versus voltage curves.

Only 26.4 nm thick optimally doped films were used in this study. Single-pass lines were written on devices across three different samples and all were largely consistent in terms of dose dependence. We focus here on making comparisons for devices patterned on the same chip. Instead of electron beam lithography used to define the bridges of varying widths, down to the nanoscale as with the bilayer samples, we fixed the bridge width at 5 μm and so there was no need for an electron beam lithography step. Rather, photolithography was used to define the four-point devices, and pattern transfer was performed by Argon ion beam etching.

Single-pass lines (Fig.4.5) were defined to be the smallest widths possible in the Zeiss built-in nanopattern generation software. We aligned to alignment marks defined for each device in the photolithographic step. Since we knew the distances from the alignment marks to the devices we could then align to the devices. In this way, the helium beam dwell time on the device during navigation and imaging was minimized. A second alignment step followed, on the periphery of the bridge itself without causing harm to the region of interest. The majority of lines were written with 1 pA emission current and 30 kV accelerating voltage.

4.4.1 Dose Units

For the line pattern writes, the helium beam is scanned across the bridge in a single pass. The beam writes lines by exposing a pitch of ultra small beam spots with a pitch of 0.25 nm which is roughly half the supposed beam diameter of 0.5 nm. In this way, it is able to approximate a continuous line since the center-to-center distance or pitch, is smaller than the assumed beam diameter. The dose administered for such a one dimensional pattern is given in units of ions per nanometer or ions / nm. For line doses, we will use these units. Area doses will be given in units of ions per square cm or ions/cm^2. One can approximate roughly the equivalent linear units from the areal dose, by dividing by a factor of 10^{14} which is simply the conversion from square nanometers to square centimeters.

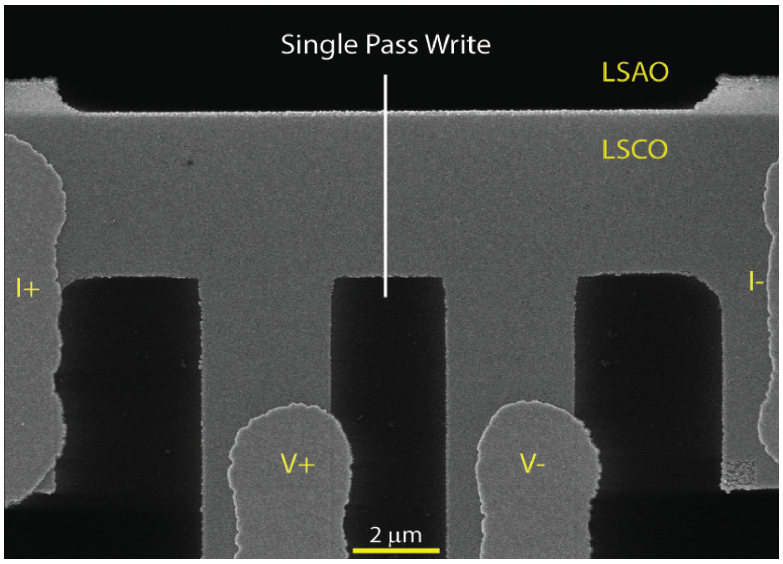

Figure 4.5: Top view schematic of a patterned tunnel junction device. A single pass Scanning Helium Ion Beam is used to write a line on a 5 μm microbridge. The write dose was varied from 10^2 ions/nm to 10^4 ions/nm. The Helium ion beam voltage was set to 30 kV.

4.4.2 Results of Single-Pass Writes To Create Tunnel Junctions

Four-probe, current biased measurements were taken after the helium ion beam patterning. The samples were mounted on chip carrier and cooled down to the cryostat base temperature of 4 K while resistance was measured. The resultant data in Fig. 4.6 shows the modified resistances of the bridges with a line write across the bridge (shown in Fig.4.5). The resistance versus temperature curve for an unpatterned bridge is shown for comparison. For doses high than a threshold dose, of 608 ions/nm, the resistivity is increased. The normal state resistance increases by up to a factor of two. For the dose of 1187 ions/nm, the highest shown here, the difference is most stark. It shows quite insulating behavior with a sharp upturn immediately after the superconducting transition where the resistance drops to a value of about 44 ohms. The 4 K resistance for that device is close to 123 Ω. In this way, we have found a line dose that will can electrically isolate the nanowire pattern and suppress superconductivity along currents paths every where by the nanowire pattern. At lower temperatures, because of the

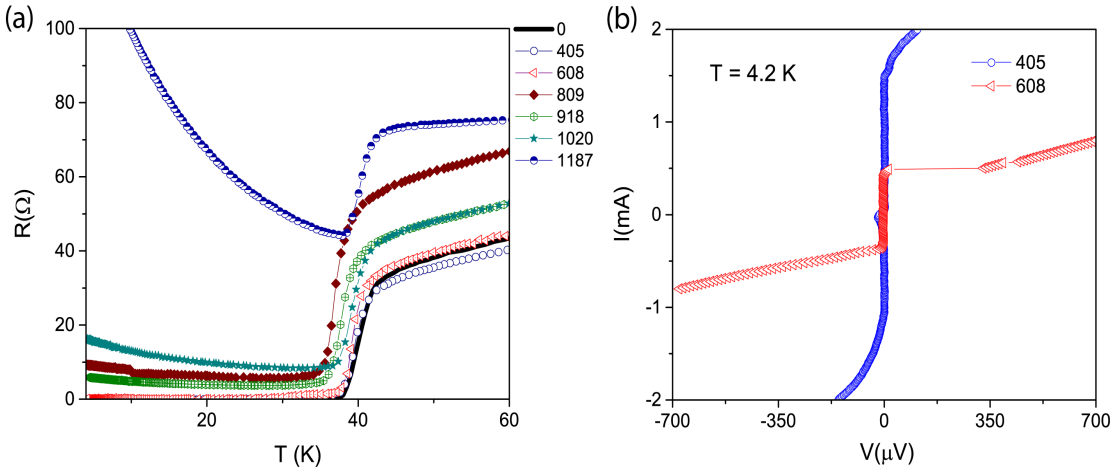

Figure 4.6: Dose units in the legend (ion/nm) (a) Resistance versus temperature measurements of different devices differing by the administered line dose. Resistance for an unpatterned bridge with 0 dose is shown for reference. Superconductivity suppressed leading to low temperature insulating behavior for doses above a dose threshold (608 ions/nm). (b) I-V characteristic for the two superconducting devices shown in panel (a) These two devices had line doses below the threshold but show diminished critical currents.

insulator temperature dependence, we expect the isolation to be much improved.

We also carried out critical current measurements. Curves in Fig. 4.6b that were insulating displayed ohmic current-voltage characteristics as expected. Therefore, only two of the devices (405 ions/nm and 608 ions/nm) whose resistance curves are seen in Fig. 4.6 are shown in the second panel. For comparison, the critical current (not shown) for the unpatterned bridge was measured and found to be at least 10 mA. The bridge with line dose of 405 ions/nm sustains a critical current of approximately 1.5 mA. For the second device, 608 ions/nm, the critical current was suppressed down to about 450 μA.

Having shown that single-pass writes (Fig.4.5), can cause the device to undergo a superconductor-to-insulator transition tuned by the line dose, we determined the approximate range of values for the dose threshold. Armed with this data, we can proceed with writing nanowire device patterns on a microbridge with dose values which would electrically isolate. In further studies, we choose values for

isolating dose of either 10^3 or 10^4 ions/nm.

4.5 Nanowire Pattern Results

4.5.1 Nanowire Pattern: Single-Pass Outline

Devices exhibited broadened superconducting as well as insulating transitions. The absolute resistance measured was higher than for the unpatterned bridge. Dips in resistance are seen at close to the bulk critical temperature when leads go superconducting. Three single-pass outline geometries were used. In pattern1, the a single horizontal line was dosed with 10^2 ions/nm. In Pattern2, 3 horizontal lines separated by 20nm were used to define the nanowire and were each written with a dose of 10^2. Pattern3, the two vertical and single horizontal lines were written with 10^3 ions/nm. Devices 3, 4, 5, 6 in Fig.4.7 were patterned with pattern2 geometry. Pattern2 geometry sought to mitigate any damage that may occur in proximity to the nanowire region by effectively barricading with 3 lines at lower doses but which together would yield proper electrical isolation to restrict current transport to the intended nanowire region. However, the gap or effective nanowire width, varied across devices 3, 4, 5, 6. The different device nanowire widths (or gaps) for those devices patterned in pattern3 geometry were as follows: device3 (50 nm), device4 (100 nm), device5 (250 nm), and device6 (200 nm). Device2 (20nm) was written in pattern1 configuration and device1 (10nm) in pattern3 configuration.

The smallest nanowire widths of 10nm and 20nm showed insulating transitions. When the bulk leads become superconducting and therefore shorted, the contribution to the measured resistance is from the patterned nanowire. The defined nanowire with widths 10 - 20 nm, appears to be insulating. The insulating behavior portends an extrinsic damaged region or perhaps an intrinsic effect of the nanowires being narrow enough to no longer sustain superconductivity. Devices 4, 5, and 6 show transitions and are all the wider devices. Device4, however, maintains a residual resistance at T = 4 K. These devices also show a second transition indicating the nanowire has lower T_c.

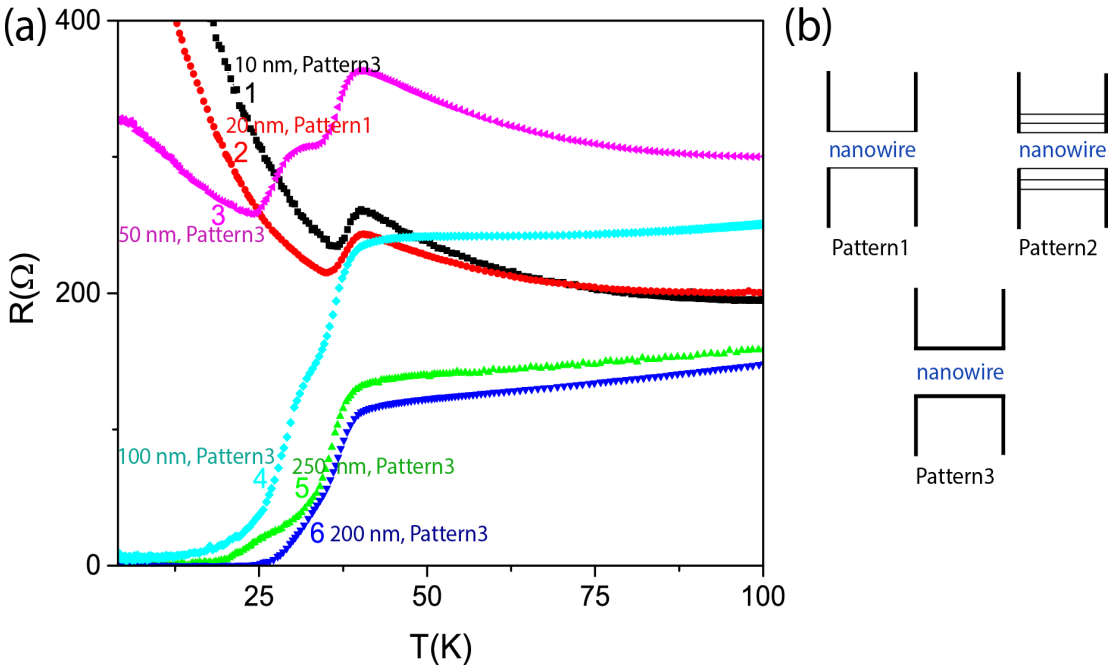

Figure 4.7: (a) Resistance versus temperature curves for nanowire devices patterned with single line dose outlines in different geometries. (b) Different outline patterns were used and are displayed in (b) The vertical lines in all the patterns: pattern1, pattern2, pattern3 written with dose 10^3 ions/nm for proper electrical isolation. Strategies for horizontal portions defining the nanowire varied. In pattern1, the a single horizontal line was dosed with 10^2 ions/nm. In Pattern2, 3 horizontal lines separated by 20nm were used to define the nanowire and were each written with a dose of 10^2. Pattern3, the two vertical and single horizontal lines were written with 10^3 ions/nm. Gap widths varied between devices, Device3 (50nm), device4 (100nm), device5 (250nm) and device6 (200nm) had pattern2 geometry. Device2 (20nm) had pattern1 geometry and finally device1 (10nm), pattern3 geometry.

In summary, the single pass outline nanowires pattern technique appears promising. The true nature of the nanowire core would require further investigation. While the helium ion beam size is 0.25 nm, the appears to be suppression of superconductivity on a length scale greater than forty times the beam size, otherwise the nanowire pattern with 10 nm width would be completely superconducting. We have shown that the for widths of several hundred nanometers show superconducting transitions, albeit broadened. The devices appeared electrically isolated as designed from the resistance values measured.

4.5.2 Nanowire Pattern: Box Outline

The nanowire patterns defined by single pass writes showed tunability of the device resistance from insulating to superconducting. We decided to investigate the second strategy of defining the nanowires by bounded boxes or rectangles of widths 50 nm each so electrical isolation can be obtained but with the use of lower overall doses to mitigate an extrinsic effects causing possible damage to the nanowire core. Nanowires were defined by rectangular boxes of height 7.5 μm and width 50 nm, replacing the single pass bound outlines used previously. We varied the dose to find ideal helium patterning conditions where the damage is localized but also isolating enough to define a nanowire. The data in Fig.4.8 shows the crossover dose from superconducting to insulator behavior to be around 1×10^{16} ions/cm^2 for this writing strategy.

It would appear that there is some damage cause by the helium ion beam in the gap region defining the nanowire in between the box writes. However, this does not agree with the 0.25 nm helium ion beam size. In the next section we pattern nanoconstriction devices with the idea of measuring the lateral extent of the patterned junction.

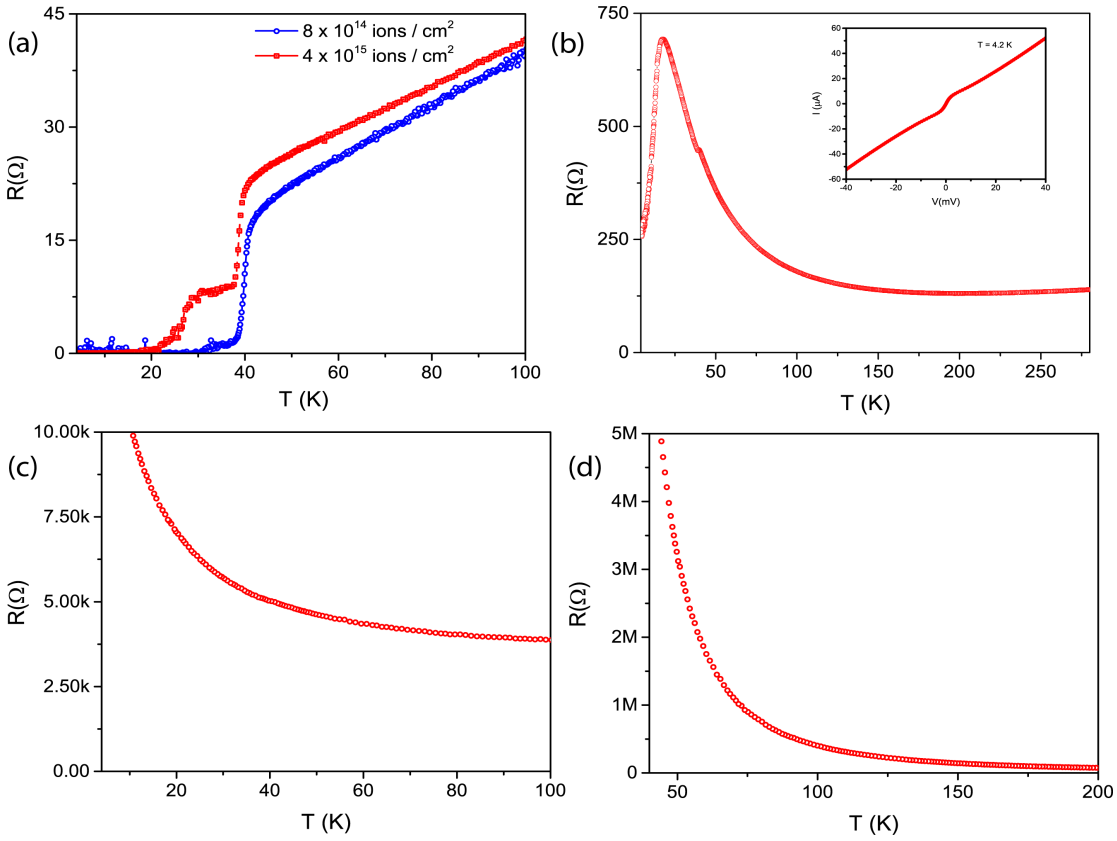

Figure 4.8: All graphs shown here were written patterns with box outlines and 100 nm gap separation. Dose was varied across (a) = 8×10^{14}, 4×10^{15} (b)= 1×10^{16} (c)= 2×10^{16}, (d)=6×10^{15} (ions/cm^2) while the box outline dimensions and the gap stayed the same. For mild doses in (a) we observed a two transitions. We believe the first transition to be for the bulk leads and the second for the damaged gap region and intended nanowire with decreased T_c. As the dose is increased and intermediary regime is reached with reentrant behavior in panel (b) and driven to insulating behavior in panels (c) and (d)

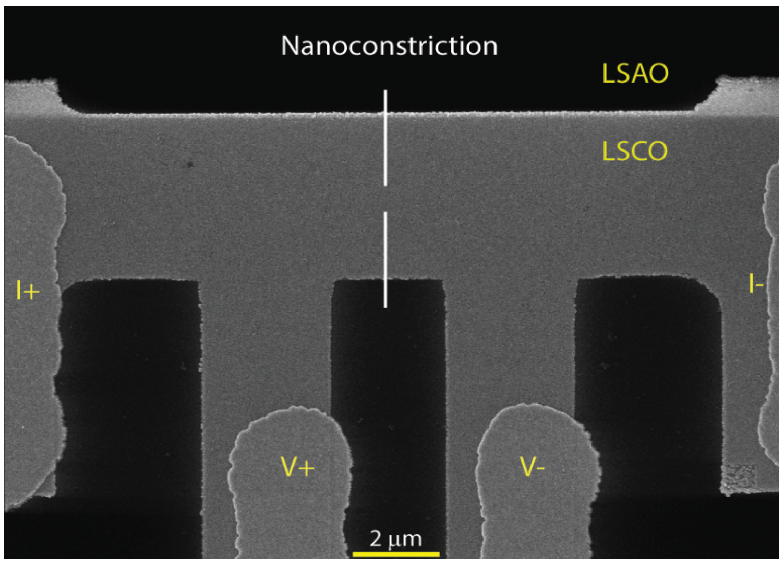

Figure 4.9: Top view annotated Helium ion microscope image of a nanoconstriction device pattern. Each line is a one pass line written with the scanning helium ion beam and separated by a gap, whose dimensions are varied. For high fluence writes that locally suppress superconductivity, as previously shown, if the gap is too small we observe insulating resistance versus temperature profile in transport. When we approach a threshold gap where the damage region from either line does not overlap, then we will have estimated the damage extent of the junction.

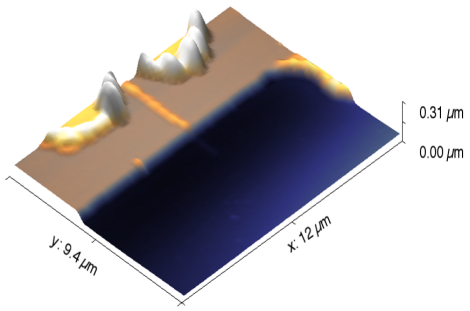

Figure 4.10: An AFM scan of a nanoconstriction device with a gap size of 80 nm. The topographic feature is 30 nm high and is clearly seen between the two Au voltage electrodes on either side of it. The origin of this strange topographic feature is not well understood. The lateral extent, across the single-pass line, is 400 nm which may explain why the smaller 80 nm design gap is not visible.

4.6 Superconductivity in Nanoconstriction Devices

The nanoconstriction pattern is shown in Fig.4.9. We carry out two single-pass writes separated by a gap, whose size we vary from 10 nm to 800 nm. We use single-pass doses we know to display insulating behavior from our previous work with single-pass writes (Fig.4.7). For the insulating line, that is, the limit of gap = 0 nm, we would measure insulating resistance versus temperature characteristics. As we increase the width gradually in across different patterned devices, we wish to cross a threshold width were we regain a superconducting transition and measure critical current. In so doing, we have an effective method of measuring lateral junction extent provide the high fluence writes create electrical isolation suppressing the superconducting transition.

We patterned 10-20 devices per chip. Here we show (Fig.4.10) the data for devices written at 1×10^4 ions/nm dose, and gap dimension of 80 nm. If the lateral extent of this dose write were less than 40

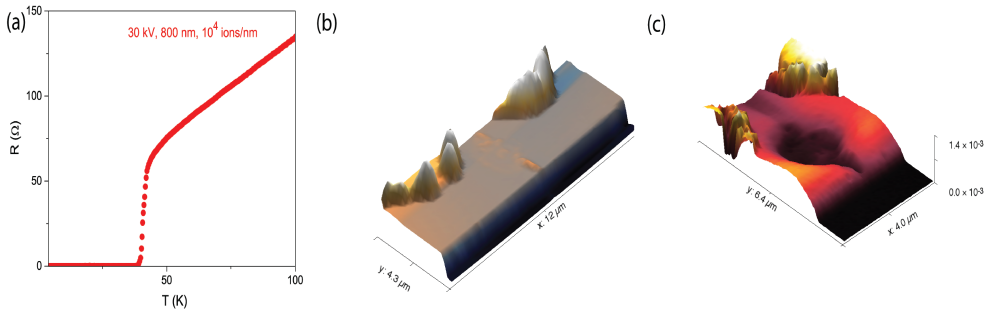

Figure 4.11: (a) Resistance versus temperature curve of device with an 800 nm wide constriction written at 1×10^4 ions/nm. (b) AFM scan shows topographic lines. The presence of topographic features where the gap was defined is quite surprising and strange. To verify the nature of the gap material (c) shows the s-SNOM data collected. This near field optical technique is sensitive to the contrast in dielectric constant between materials. In (c) please note the s-SNOM image is not topographic but indicates the relative differences in dielectric constant at the damaged site versus the surrounding areas. (b) and (c) are similarly oriented. The voltage electrodes are seen flanking either side of the patterned nanoconstriction device in both AFM (b) and SNOM (c) images.

nm, we would expect superconducting transition. However, our transport measurements show completely insulating behavior in the MΩ level. We performed AFM and s-SNOM (scanning near-field optical microscopy) in order to characterize the effects of scanning the sub-nm focused He beam on the High-T_c film for another device written with a 1×10^4 ions/nm dose but this time a nanoconstriction gap size of 400 nm (Fig.4.11). We also observe a topographic feature with a height of 20-30 nm and with a lateral extent of 400 nm.

The s-SNOM data was collected by Dr. Adrian Gozar at Brookhaven National Laboratory. S-NOM is a versatile optical imaging technique which circumvents the diffraction barrier by detecting the light scattered from a sharp probing tip oscillating above the specimen surface. The technique relies on the interaction between the sample and the enhanced electromagnetic field induced by antenna effects in the proximity of a sharp metallic atomic force microscope (AFM). The size of the tip also determines the spatial resolution. This electromagnetic coupling allows extraction of the nanoscale dielectric properties of metallic and/or insulating phases. Our data were taken in what is called the homodyne detection scheme where the measured detector output is the result of the interference be-

tween the true near field signal and a reference beam which in this case is just the background light generated by the illumination of the entire AFM tip body and/or neighboring regions of the sample. The near-field signal is mediated by the evanescent components of the electric field in the proximity of the tip. The typical depth probing range can be estimated from approach curves and is of the order of 20-50 nm. The SNOM results (Fig.4.11c) show dielectric contrast along the trace generated by the He beam path and it correlates with the AFM data. Line profiles show an unexpected and strange, large circular region where the gap was defined in the pattern. The data is evidence that the mid-infrared optical properties of the regions exposed to 30 keV He ion beams changed it dramatically in a way we have yet to fully understand. We are clearly dealing with a very different material from the optimally doped High-T_c film.

Techniques such as this have a potential to be game-changing. Being able to write narrow tunnel junction in complex oxides could open pathways to interesting functional devices[55]. However, there remains much to be investigate at these high fluence rates. With a high fluence rate, superconductivity is locally suppressed. This is most useful if the damaged region is localized to a few nanometers. With the beam spot size of the Helium ion beam being quite low, the expectation of direct patterning fine lines should be investigated further.

4.7 Conclusion

We have patterned superconducting tunnel junctions by varying the helium ion beam write doses. We found the threshold doses for tuning the microbridges from superconductor to insulators. Our nanowire devices exhibited damage from the helium ion fluence. We investigated this further by carrying out AFM and s-SNOM scans. At high dose (10^3 - 10^4 ions/nm), there is a sharp changed induced in device characteristic: AFM images show topographic helium induced mounds created using single slit devices, we assess the tunnel junction lateral extent.

5

LSCO Bilayer Films On Vicinal Substrates

Nanofabrication by electron beam lithography or utilizing a direct nanopatterning scanning helium ion beam are useful techniques for small area writes. Applying these techniques to larger areas would require long write times that may not be feasible, depending on the application. In addition, both techniques require charged particles interacting with the film which can cause deleterious effects. As for the helium ion beam case, the nature of these charge ion interactions with the material of interest may not be amenable to traditional models as shown for high fluence rates of helium ion beam expo-

sure (chapter 4). Large scale nanopatterning techniques utilizing nanoimprint lithography[57], templating[58] and chemical treatments[59,60], have been thoroughly researched. However, for the niche application of patterning superconducting nanowire with pristine quality as well as Josephson Junctions with high $I_c R_n$ products from avoidance of lithographic damage, the above techniques have drawbacks. The templating and nanoimprint techniques introduces the nanostructures to an ion milling process while the chemical treatment method patterns alumina substrates that are not lattice matched for high quality LSCO cuprate growth. In this chapter, we devise a method for large scale patterning of superconducting junctions and nanowires. We examine its merits and propose further improvements.

5.1 Novel Method for Nanowire Patterning: *Sunray* Geometry

The $LaSrAlO_4$ substrates used for our MBE growth can be either flat or tilted (vicinal), that is, miscut. The terrace widths can be controlled depending on the small miscut angle. Higher values of miscut angle yielding narrower terraces.

When bilayer samples of non-superconducting overdoped metallic LSCO and insulating LCO are combined[20] the interface has been shown to exhibit superconductivity. These heterostructures can be engineered with a clearly defined number of metallic layers as well as insulating layers. They can be grown in different orders as well. The highest critical temperatures are seen with bilayers in which the metallic shunt is grown first atop the substrate. This is the configuration utilized for samples examined in this experiment. Such bilayer samples when grown atop tilted substrates have the interface layer interrupted by the substrate step height. The step height is typically a unit cell length in that particular crystallographic direction for the best atomically smooth substrates. As a result of this discontinuity of the interface layer across the entire of the film, nanowires are created with widths equivalent to the substrate terrace widths and nanowire thickness that of the interface which is 0.66 nm. Incidentally, by changing the miscut angle of the substrate one effectively controls the width

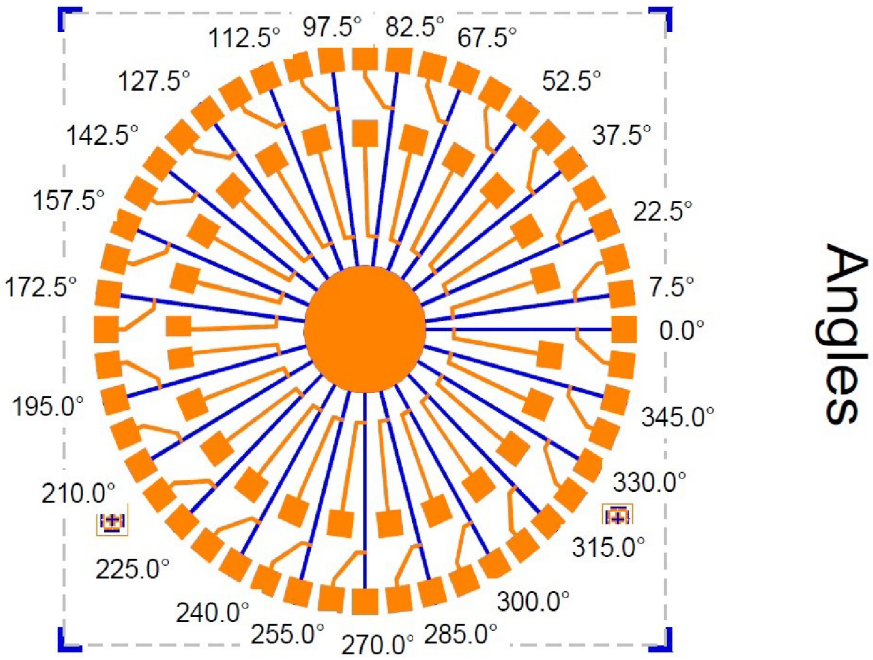

Figure 5.1: Drawing of the *sunray* Pattern, defined by photolithography. Strips patterned at varying angles to measure the critical current anisotropy. Strip widths are typically 5 μm. Devices are roughly 15° apart. We also patterned samples with narrower angular spacing of 4° separation between device rays. Those results are discussed in the text.

of the nanowires created. In such a way, large scale nanowires are made. Because of the discontinuity of affecting the superconducting interface, the superconducting nanowires may be coupled across terraces by Josephson coupling. Josephson junctions can then be feasibly made on a large scale with uniformity with this technique.

Determining the lengths of nanowires made this way is a more involved issue. The lengths of the nanowires depend then on the terrace lengths. Substrates such as STO [61] can be treated to straight terraces on the atomic scale with minimal line edge roughness. In fact, STO substrates can be treated even to have single terminations in TiO_2. Here, we use LSAO substrates nonetheless, but the technique will be fine tuned with STO substrates in continuing studies.

To test the effectiveness of the technique, bilayer films were grown by ALL-MBE and fabricated by photolithography into strips or rays of several microns at different angles, in a pattern what we call a *sunray* pattern Fig.5.1. The 0° and 180° angles correspond to strips aligned parallel to the terraces while 90° and 270° correspond to strips running perpendicularly across the substrate terraces. Post film growth, the terraces are also observed on the bilayer thin films. If the bilayers indeed exhibit this discontinuity of the superconducting interface layer across terraces, then we ought to observed different transport properties at the different angles since the effective nanowire cross-section would vary with angle. Critical current anisotropies were measured across multiple angles. Close to 90 angles were measured per sample and up to 5 samples were characterized with at least two fully characterized for resistance and critical current anisotropies. The photomask was made and photolithography carried out by Dr. Anthony Bollinger at BNL. I performed the transport measurements.

5.2 Anisotropic Critical Currents

Extensive measurements were carried out for each angle, across multiple samples. More importantly, critical currents, and their angular variations were measured at T = 4.2 K for all the devices character-

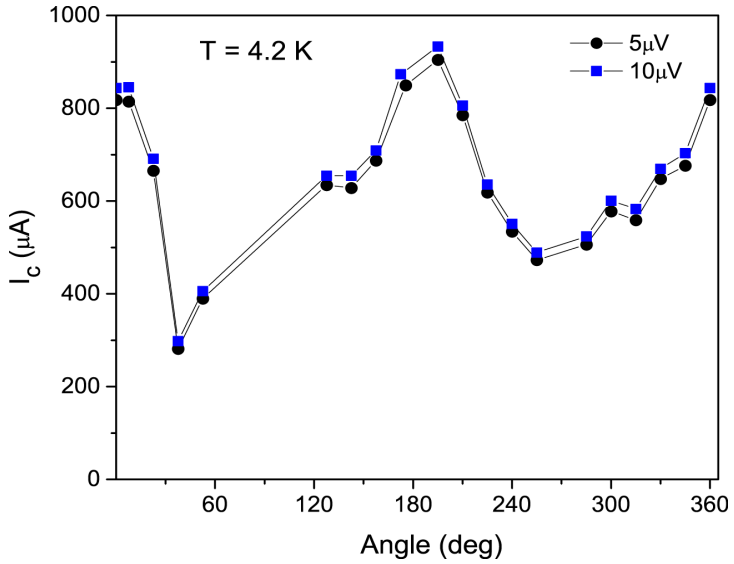

Figure 5.2: Critical current versus angle plot showing anisotropy along different ray directions. Sample is a 10M + 10I bilayer grown on a 1.9° miscut substrate. The critical current values were measured at T = 4.2 K. Devices were patterned roughly every 15°.

ized. For some particular rays that warranted further characterization, such as close to 0°, or 90° rays, the temperature dependence of the critical current was also measured. Sample1568 (T_c = 31 K) shown in 5.2 was grown on a 1.9° miscut angle with an expected terrace width of 18 nm. Its heterostructure consists of 10 insulating monolayers of LCO atop 10 metallic layers Sr-doped (x=0.44) LSCO, that is (10M + 10I). The rays were patterned every 15°, making for 24 devices.

To further confirm these results, another sample(sample1612, T_c = 37 K) with similar heterostructure of 10M + 10I bilayer, was grown on a 1.9° miscut substrate. This time, the photolithography pattern was modified to include denser rays, only 4 degrees apart to obtain a finer angular distribution over the previous sample with devices patterned every 15°. For the new sample, 90 devices were available for measurement, and 81 devices were measured. 5.3 shows the resistance versus temperature characteristic of these devices measured with same bias currents. Note that the high temperature resistances are dominated by the metallic shunt. In addition we also characterized the critical current anisotropy versus angle see in ??.

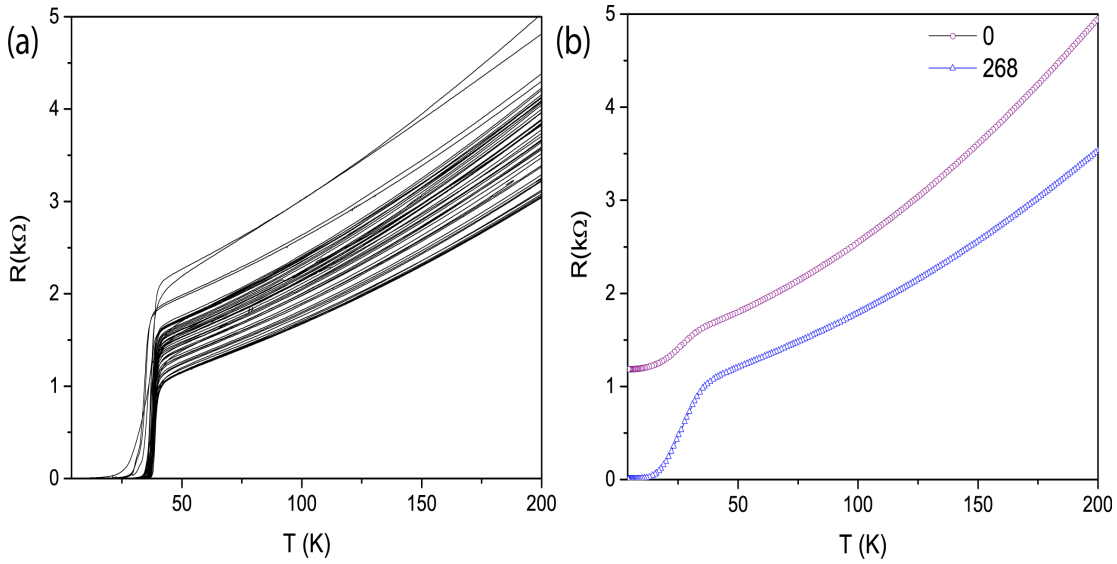

Figure 5.3: Second sample is a 10M + 10I bilayer grown on a 1.9° miscut substrate.(a) Resistance versus temperature for 50 angles measured with a current bias of 1μA. Devices were patterned every 4°. (b) Anisotropy between the device ray parallel to the terrace and those at normal angles to the terrace when biased at 1 mA. 1 mA was chosen since it was larger than the critical current of the ray at 268°. This bias current value of 1 mA is lower than the critical current of the 0° ray thereby yielding the plot seen. Therefore, parallel to the terrace shows superconductivity and perpendicular direction shows finite resistance, on the same film.

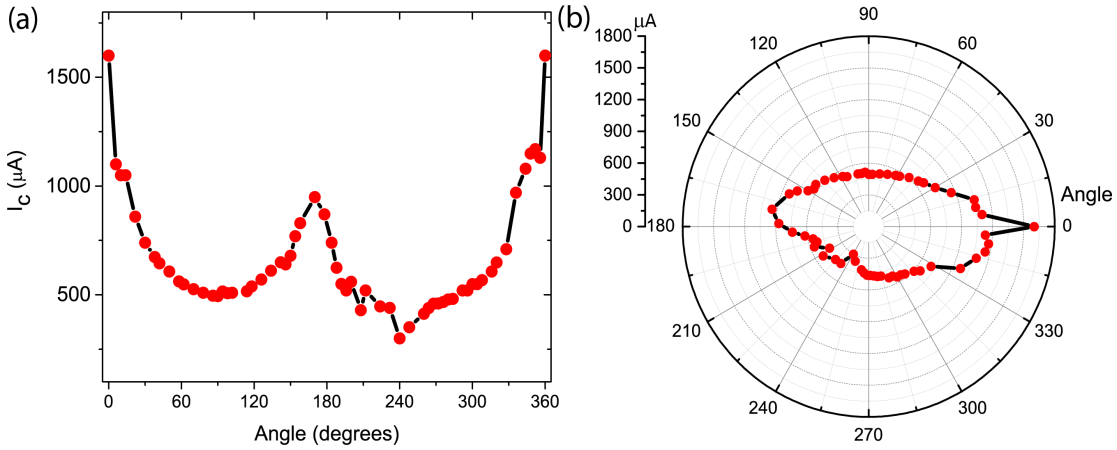

Figure 5.4: Sample is a 10M + 10I bilayer grown on a 1.9° miscut substrate. Devices were patterned roughly every 4°. I_c measured at T = 4.2 K for all device rays. (a) Linear plot of the critical current versus angle. The graph clearly shows I_c anisotropy along the different ray directions with angles close to the terrace parallel achieving either global or local critical current maxima. (b) A polar curve of (a) to show the geometric effect more clearly. There is a distortion in the plot which may be due to slight misalignment of the photolithographic patterning step with the true terrace parallel direction

5.3 TEM Characterization

Post-growth, AFM measurements were also taken. These measurements showed some step bunching. We suspect the bunching cannot permeate through to the superconducting interface or the substrate interface. To clarify this, the sample was prepped and imaged with a transmission electron microscope (TEM). The TEM portion of the study was performed by Dr. Myung-Geun Han at Brookhaven National Laboratory.

The TEM results clearly show steps along both interfaces indicating step bunching is a surface effect in our sample and does not propagate through to the pertinent superconducting layer. Step bunching is an amalgamation of several steps making them wider and taller than the native steps of the substrate.

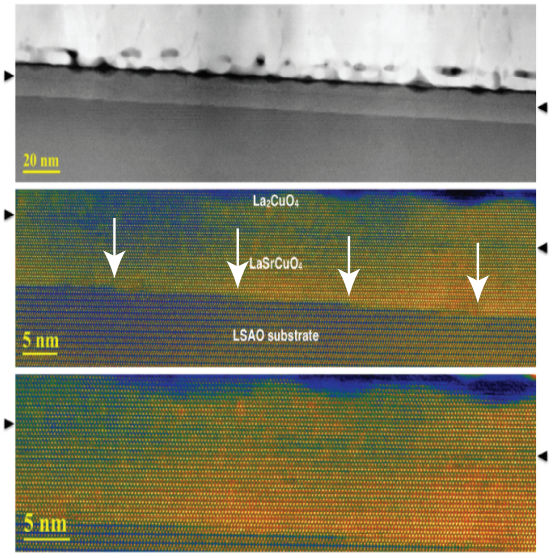

Figure 5.5: TEM image of sample along (110) zone axis.

5.4 Engineering The Anisotropy

To further show control of the technique, a key metric that can be adjusted is the anisotropy between the 0° and 90° rays of the patterned film. Bilayer samples were purposefully engineered to enhance this anisotropy. Because Zn is well known to suppress superconductivity in the cuprates, if a bilayer film was grown with a fraction of any terrace width consisting of Zn-doped LSCO , then transport along the perpendicular direction would be suppressed. The film growth technique required to achieve this is challenging. Films were grown in step-flow growth mode in the Oxide MBE machine to achieve this lateral heterostructure to enhance anisotropy. Nanowire widths can be further controlled in this fashion by adjusting the lateral percentage of the terrace occupied by the Zn-doped LSCO film. Transport measurements of the critical current in the 0° direction and the normal direction show in fact disparate critical currents as seen in the Fig.5.6b.

Another alternative to using Zn-doped to enhance anisotropy is using LSAO as the terrace buffer. Because LSAO is insulating, it will naturally enhance anisotropy is simply to use insulating LSAO. In

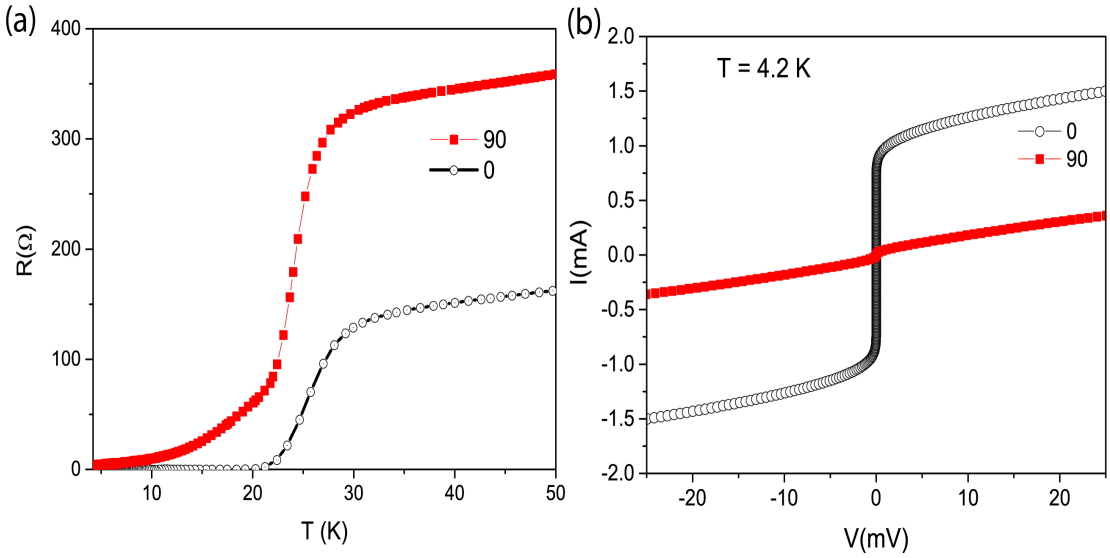

Figure 5.6: Sample is a 10M + 10I bilayer grown on a 3.8 degree miscut substrate with Zn-LSCO buffer on part of the terrace.(a) Resistance versus temperature for 0 and 90 degree angles. 0 degree is superconducting and 90 degree is not.(b) Critical current anisotropy between 0 and 90 degrees is evident.

this scheme, a fraction of the terrace width would contain the normal bilayer heterostructure, untainted, and the remainder would contain LSAO. More work needs to be done in properly controlling either a Zn-doped or LSAO buffer layer on a terrace. Work is currently underway to image by TEM those samples grown by step-flow growth mode, to determine precise lateral distribution of the buffer layers. In step-flow growth mode, atoms land on the surface and diffuse to the step edge since the mean free path is longer than the terrace width which is defined by a choice of miscut angle. Moreover, the initial substrates used must have terraces with low line edge roughness, and are 100s of microns long. Future work will rely heavily on straightening and lengthening the terraces with proper surface chemical treatments and annealing for the right substrate.

5.5 Conclusion and Future Work

In summary, we proposed, developed and evaluated a novel procedure for potential pathway towards large scale patterning of nanowires and junctions by taking advantage of bilayer films sustaining superconductivity and grown on vicinal substrates of varying tilt angles.

6

Conclusion

Fabricating nanostructures from high temperature cuprate superconductors has been a challenging task because of their short coherence length and their high sensitivity to disorder. Motivated by the fundamental physics question of whether telegraph noise signals observed in YBCO cuprate nanostructures are universal to the cuprates or specific to YBCO family, we set out to develop the nanofabrication technology required to create nanostructures in which such questions can be answered confidently. The answer, null or not, will have implications on what we understand to be the fundamental

excitations in these class of materials. If similar purported noise signatures of stripe physics and pseudogap physics are not observed in a host of materials systems then it can be said these theories do not occupy a paramount position on the Mount Olympus of high temperature superconductivity theories.

We fabricated sub-100 nm nanowires from bilayer and optimally doped non-bilayer thin films after pinpointing the ion milling step to be crucial. We observed high critical current densities for the bilayer structures and for structures patterned with an ex situ Au cap. We found optimally doped nanowire structures to be more robust to the wears and tears of the lithographic process. For underdoped samples we could pattern superconducting wires down 400 nm, albeit not with a high throughput. Other novel methods were attempted, and evaluated to create pristine nanostructures. With the scanning helium ion beam technique, we found we could create superconducting tunnel junctions, which are tuned insulating with high helium fluence writes. For extremely high doses we found topographic features. We found the use of nanoconstrictions useful in evaluating lateral extent in the high fluence writes.

More work needs to be done on large scale patterning of nanowires and junctions using bilayer films grown on vicinal substrates. Quite a bit of data has been collected to lead the way about necessary next steps.

With sub-100 nm nanowires, the next step has already begun in getting back to answering the fundamental physics question at hand about nematic domains. Cross correlation measurements proposed by Professors Carlson and Dahmen to test the anisotropy of the purported fluctuating domains in the LSCO cuprate is the clear way forward.

A

Fabrication Recipes Explored

A.1 Recipe for Nanowire Fabrication

A.1.1 MA-N2400 Series Negative Tone Resist

- Bake thin film for 5 minutes at 90° C
- Spin MAN-2403 resist at 3000 RPM for 45 seconds
- Acceleration for spin cycle 1500 RPM lasting 2 seconds

- Bake resist for 1 minute at 90°C
- Electron beam current for writing less than 1 nA
- Nanowire area dose: 300 - 400 μC/cm^2
- Larger pads and contact dose: 100-200 μC/cm$_2$
- Develop film in MAD-525 solution
- Rinse in deionized water for 2 minutes
- Dry with a nitrogen
- Hard bake at 90°C - 100°C is optional

A.1.2 Sub-20 nm Lines in HSQ and Carbon

Exposures were carried out on the structure: LSCO / Au(50 nm) / Carbon (40 nm).

Pattern transfer into carbon was carried out successfully at these linewidths.

- Bake thin film for 10 minutes at 90° C
- Spin HMDS for adhesion at 3000 RPM for 30 seconds
- Bake for 3 minutes at 90°C
- Spin HSQ 2% at 6000 RPM for 45 seconds
- Post applied bake for 3 minutes at 90° C
- Electron beam current for writing, 100 pA
- Nanowire area dose: 60 - 75 mC/cm^2 for 0.5 - 1.75 nm shot pitches
- Develop film in AZ-400K 45 seconds
- Rinse in deionized water for 10 seconds
- Dry with nitrogen

The developer used, TMAH-based, was key. I initially tested the salty developer solution (NaOH-NaCl 1:4) but found residue on the sample surface. The carbon films in this study were deposited

using an electron beam evaporator. Process improvement can be made with sputtered carbon films instead for more uniform carbon coating and conformation. Furthermore, the shot pitches and beam currents used were intentional. I ran simulations on the JEOL e-beam tool for the estimated beam spot size dependence on current value, mode (3 or 6) in JEOL speak, aperture (25 μm or 60 μm). The e-beam writing condition was then chosen with an overlapping beam spot pitch model in mind. Wire widths were designed as multiples of the simulated beam spot sizes and shot pitch.

A.1.3 Sub-100 nm PMMA Tone Reversal Lines

- Bake thin film for 5 minutes at 100° C
- Spin PMMA C496K 1:2 4000 RPM
- Bake for 5 minutes at 100-180°C
- Spin HSQ 2% at 6000 RPM for 45 seconds
- Post applied bake for 3 minutes at 90° C
- Electron beam current for writing, 1-2 nA
- Nanowire area dose: 20-24 mC/cm^2
- Develop film in MIBK for 1 minute
- Rinse in IPA for 15 seconds
- Dry with nitrogen
- Fig.A.1 shows the recipe post processing

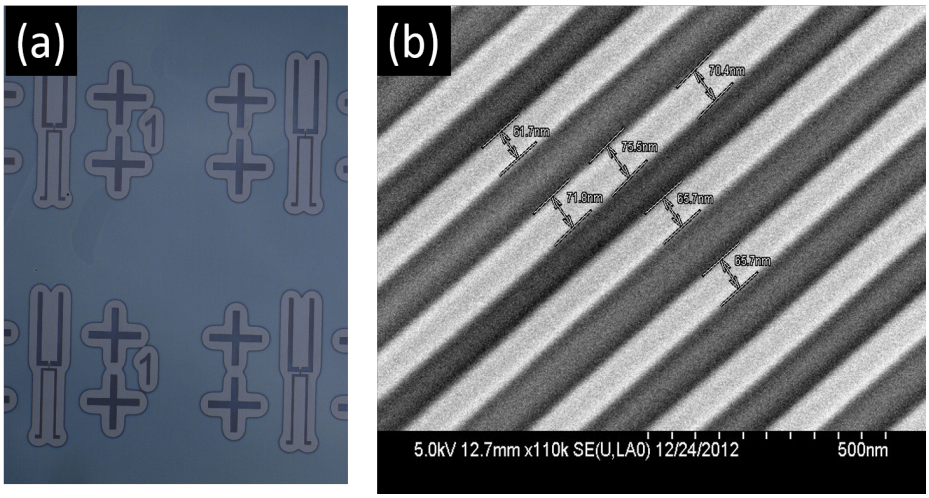

Figure A.1: (a) Optical image showing image reversal of positive PMMA when the exposure dose is high. The dark blue regions are the negative tone PMMA resist, the light blue regions are positive PMMA resist that have not tone reversed because of distance from exposed region. (b) SEM image of an array of lines written with PMMA tone reversal having widths less than 80 nm.

References

[1] Dirk Van Delft and Peter Kes. The discovery of superconductivity. *Physics Today*, 63(9):38, 2010.

[2] R. Meissner, W. and Ochsenfeld. Ein neuer effekt bein eintritt ber supraleitfahigkeit. *Die Naturwissenschaften*, 21(September):787–788, 1933.

[3] A A Abrikosov. Nobel Lecture: Type-II superconductors and the vortex lattice. *Reviews of Modern Physics*, 76(December):975–979, 2004.

[4] J. Bardeen. Theory of superconductivity. *Physica*, 24:S27–S34, 1958.

[5] M. Tinkham. Energy gap interpretation of experiments on infrared transmission through superconducting films. *Physical Review*, 104(3):845–846, 1956.

[6] Ivar Giaever. Electron Tunneling Between Two Superconductors. *Physical Review Letters*, 5(10):464–466, 1960.

[7] B D Josephson. Possible new effects in superconductive tunneling. *Physics Letters*, 1(July):7–9, 1962.

[8] Ilija Zeljkovic. *Disorders in High-Temperature Supercondu ors using Scanning Tunneling Microscopy*. PhD thesis, Harvard University, 2013.

[9] J G Bednorz and K A Miiller. Condensed Matt Possible High T c Superconductivity in the Ba - L a - C u - o System. *Zeitschrift fur Physik B Condensed Matter*, 193(64):189–193, 1986.

[10] Wu, M. K. and Ashburn, J. R. and Torng, C. J. and Hor, P. H. and Meng, R. L. and Gao, L. and Huang, Z. J. and Wang, Y. Q. and Chu, C. W. superconductivity at 93K in a new mixed phase YBACUO compound system at ambient pressure. *Physical Review Letters*, 58(9):908–910, 1987.

[11] T. Timusk and B. W. Statt. The pseudogap in high-temperature superconductors: an experimental survey. *Rep. Prog. Phys.*, 61:54, 1999.

[12] D Elbio. Complexity in Strongly Correlated Systems. *Science*, 309(July):257–262, 2005.

[13] E. W. Carlson, V. J. Emery, S. A. Kivelson, and D. Orgad. Concepts in high temperature superconductivity. *Superconductivity*, pages 1225–1348, 2008.

[14] J Zaanen and O Gunnarsson. Charged magnetic domain lines and the magnetism of high T_c oxides. *Phys. Rev. B*, 40(10):7391, 1989.

[15] V J Emery, S A Kivelson, and J M Tranquada. Perspective stripe phases in high temperature sperconductors. *Proc. Natl. Acad. Sci.*, 96(August):8814–8817, 1999.

[16] J E Hoffman, E W Hudson, K M Lang, V Madhavan, H Eisaki, S Uchida, and J C Davis. A four unit cell periodic pattern of quasi-particle states surrounding vortex cores in Bi2Sr2CaCu2O8+delta. *Science (New York, N.Y.)*, 295(5554):466–469, 2002.

[17] Colin V Parker, Pegor Aynajian, Eduardo H da Silva Neto, Aakash Pushp, Shimpei Ono, Jinsheng Wen, Zhijun Xu, Genda Gu, and Ali Yazdani. Fluctuating stripes at the onset of the pseudogap in the high-T(c) superconductor Bi(2)Sr(2)CaCu(2)O(8+x). *Nature*, 468(7324):677–680, 2010.

[18] John a. Robertson, Steven a. Kivelson, Eduardo Fradkin, Alan C. Fang, and Aharon Kapitulnik. Distinguishing patterns of charge order: Stripes or checkerboards. *Physical Review B - Condensed Matter and Materials Physics*, 74(13):1–10, 2006.

[19] R Comin, A Frano, M M Yee, Y Yoshida, H Eisaki, E Schierle, E Weschke, R Sutarto, F He, A Soumyanarayanan, Yang He, M Le Tacon, I S Elfimov, Jennifer E Hoffman, G A Sawatzky, B Keimer, and A Damascelli. Charge Order Driven by Fermi-Arc Instability in Bi 2 Sr 2 − x La x CuO 6 + d. 343(January):390–392, 2014.

[20] A Gozar, G Logvenov, and LF Kourkoutis. High-temperature interface superconductivity between metallic and insulating copper oxides. *Nature*, 455(October):10–13, 2008.

[21] N.E. Litombe, A.T. Bollinger, J.E. Hoffman, and I. Božović. La2−xSrxCuO4 superconductor nanowire devices. *Physica C*, 4:2–6, 2014.

[22] J. A. Bonetti, D. S. Caplan, D. J. Van Harlingen, and M. B. Weissman. Electronic transport in underdoped YBa2Cu3O7-delta nanowires: evidence for fluctuating domain structures. *Physical review letters*, 93(8):087002, 2004.

[23] G Papari, F Carillo, D Stornaiuolo, L Longobardi, F Beltram, and F Tafuri. High critical current density and scaling of phase-slip processes in YBaCuO nanowires. *Superconductor Science and Technology*, 25(3):035011, 2012.

[24] R. Arpaia, S. Nawaz, F. Lombardi, and T. Bauch. Improved Nanopatterning for YBCO Nanowires Approaching the Depairing Current. *IEEE Transactions on Applied Superconductivity*, 23(3):1101505–1101505, June 2013.

[25] Riccardo Arpaia, Shahid Nawaz, Floriana Lombardi, and Thilo Bauch. Improved nanopatterning for YBCO nanowires approaching the depairing current. *IEEE Transactions on Applied Superconductivity*, 23(3), 2013.

[26] S. Nawaz, R. Arpaia, F. Lombardi, and T. Bauch. Microwave response of superconducting YBa2Cu3O7−δ nanowire bridges sustaining the critical depairing current: Evidence of Josephson-like behavior. *Physical Review Letters*, 110(16):1–5, 2013.

[27] D. Levi, A. Shaulov, G. Koren, and Y. Yeshurun. Magnetoresistance anomalies in ultra-thin granular YBa2Cu3O7−δ bridges. *Physica C: Superconductivity and its Applications*, 495:39–43, 2013.

[28] D. Levi, A. Shaulov, A. Frydman, G. Koren, B. Ya. Shapiro, and Y. Yeshurun. Periodic negative magnetoresistance in granular YBa 2 Cu 3 O 7− δ nanowires. *Europhys. Lett.*, 101:67005, 2013.

[29] Ilya Sochnikov, Avner Shaulov, Yosef Yeshurun, Gennady Logvenov, and Ivan Bozović. Large oscillations of the magnetoresistance in nanopatterned high-temperature superconducting films. *Nature nanotechnology*, 5(7):516–519, 2010.

[30] Alex D Semenov, Gregory N Gol'tsman, and Alexander A Korneev. Quantum detection by current carrying superconducting film. *Physica C: Superconductivity*, 351(4):349–356, 2001.

[31] C.M. Natarajan, M.G. Tanner, and R. Hadfield. Superconducting nanowire single-photon detectors: physics and applications. *Supercond. Sci. Technol.*, 063001, 2012.

[32] K. K. Likharev. *Dynamics of Josephson junctions and circuits*. Gordon and Breach Science Publishers, 1986.

[33] KY Arutyunov, DS Golubev, and AD Zaikin. Superconductivity in one dimension. *Physics Reports*, 464:1–70, 2008.

[34] A.T. Bollinger, R. C. Dinsmore, A. Rogachev, and A. Bezryadin. Determination of the superconductor-insulator phase diagram for one-dimensional wires. *Physical Review Letters*, 101(22):1–4, 2008.

[35] A. Bezryadin, C. N. Lau, and M. Tinkham. Quantum suppression of superconductivity in ultrathin nanowires. 1760(1760):14, 2000.

[36] C N Lau, N Markovic, M Bockrath, A Bezryadin, and M Tinkham. Quantum phase slips in superconducting nanowires. *Physical review letters*, 87(21):217003, 2001.

[37] Ke Xu and James R Heath. Long Highly Ordered High Tc Superconductor Nanowire Arrays. *Nano letters*, 8(1):136–141, 2008.

[38] F. Carillo, G. M De Luca, D. Montemurro, G. Papari, M. Salluzzo, D. Stornaiuolo, F. Tafuri, and F. Beltram. Coherent transport in extremely underdoped Nd1.2Ba1.8Cu3Oz nanostructures. *New Journal of Physics*, 14, 2012.

[39] D. S. Caplan, V. Orlyanchik, M. B. Weissman, D. J. Van Harlingen, E. H. Fradkin, M. J. Hinton, and T. R. Lemberger. Anomalous noise in the pseudogap regime of YBa2Cu3O7−δ. *Physical Review Letters*, 104(17):6–9, 2010.

[40] N.E. Litombe, D. Massarotti, A.T. Bollinger, F. Tafuri, X. He, I Božović, and J.E. Hoffman. Mesoscopic properties of superconducting Lanthanum cuprate nanowires. 2015.

[41] D. E. McCumber and B. I. Halperin. Time scale of intrinsic resistive fluctuations in thin superconducting wires. *Physical Review B*, 1(3):1054–1070, 1970.

[42] J. S. Langer and Vinay Ambegaokar. Intrinsic resistive transition in narrow superconducting channels. *Physical Review*, 164(2):498–510, 1967.

[43] A. J. Pauza, W. E. Booij, K. Herrmann, D. F. Moore, M. G. Blamire, D. a. Rudman, and L. R. Vale. Electron-beam damaged high-temperature superconductor Josephson junctions. *Journal of Applied Physics*, 82(11):5612, 1997.

[44] E. W. Carlson, K. A. Dahmen, E. Fradkin, and S. A. Kivelson. Hysteresis and noise from electronic nematicity in high-temperature superconductors. *Physical Review Letters*, 96(9):1–4, 2006.

[45] H A Mook and F Dogan. Charge fluctuations in Yba2Cu3O7-x high-temperature superconductors. *Nature*, 401:145–147, 1999.

[46] H. Mook, Pengcheng Dai, and F. Doğan. Charge and Spin Structure in YBa2Cu3O6.35. *Physical Review Letters*, 88(9):1–4, 2002.

[47] S. A. Kivelson, E. Fradkin, V. Oganesyan, I. P. Bindloss, J. M. Tranquada, A. Kapitulnik, and C. Howald. How to detect fluctuating order in the high-temperature superconductors. 75(October):43, 2002.

[48] H. L. Hortensius, E. F C Driessen, T. M. Klapwijk, K. K. Berggren, and J. R. Clem. Critical-current reduction in thin superconducting wires due to current crowding. *Applied Physics Letters*, 100(18):3–7, 2012.

[49] Mohsen K. Akhlaghi, Haig Atikian, Amin Eftekharian, Marko Loncar, and A. Hamed Majedi. Reduced dark counts in optimized geometries for superconducting nanowire single photon detectors. *Optics Express*, 20(21):23610, 2012.

[50] D. Henrich, P. Reichensperger, M. Hofherr, J. M. Meckbach, K. Il'In, M. Siegel, A. Semenov, A. Zotova, and D. Yu Vodolazov. Geometry-induced reduction of the critical current in

superconducting nanowires. *Physical Review B - Condensed Matter and Materials Physics*, 86(14):1–5, 2012.

[51] John R. Clem and Karl K. Berggren. Geometry-dependent critical currents in superconducting nanocircuits. *Physical Review B - Condensed Matter and Materials Physics*, 84(17):1–27, 2011.

[52] N.E. Litombe, A.T. Bollinger, A. Gozar, C. Huynh, X. He, X. Leng, J.E. Hoffman, and I Božović. Superconductivity in Cuprate Nanoconstriction Devices Patterned by Helium Ion Beam. 2015.

[53] N.E. Litombe, A.T. Bollinger, A. Gozar, C. Huynh, X. He, X. Leng, J.E. Hoffman, and I Božović. Helium Ion Beam Patterning of Tunnel Junctions in LSCO Cuprates. 2015.

[54] Noé Curtz, Edmond Koller, Hugo Zbinden, Michel Decroux, Louis Antognazza, Ø ystein Fischer, and Nicolas Gisin. Patterning of ultrathin YBCO nanowires using a new focused-ion-beam process. *Superconductor Science and Technology*, 045015:13, 2010.

[55] Shane a. Cybart, E. Y. Cho, T. J. Wong, Björn H. Wehlin, Meng K. Ma, Chuong Huynh, and R. C. Dynes. Nano Josephson superconducting tunnel junctions in YBa2Cu3O7–δ directly patterned with a focused helium ion beam. *Nature Nanotechnology*, (April):1–5, 2015.

[56] B. W. Ward, John a. Notte, and N. P. Economou. Helium ion microscope: A new tool for nanoscale microscopy and metrology. *Journal of Vacuum Science & Technology B: Microelectronics and Nanometer Structures*, 24(6):2871, 2006.

[57] Stephen Y. Chou. Nanoimprint lithography. *Journal of Vacuum Science & Technology B: Microelectronics and Nanometer Structures*, 14(6):4129, 1996.

[58] Ke Xu and James R Heath. Long, highly-ordered high-temperature superconductor nanowire arrays. *Nano letters*, 2008.

[59] J H Yuan, F Y He, D C Sun, and X H Xia. A simple method for preparation of through-hole porous anodic alumina membrane. *Chemistry of Materials*, 16(10):1841–1844, 2004.

[60] Dongmok Whang, Song Jin, Yue Wu, and Charles M. Lieber. Large-scale hierarchical organization of nanowire arrays for integrated nanosystems. *Nano Letters*, 3(9):1255–1259, 2003.

[61] M. Kareev, S. Prosandeev, J. Liu, C. Gan, a. Kareev, J. W. Freeland, Min Xiao, and J. Chakhalian. Atomic control and characterization of surface defect states of TiO_2 terminated $SrTiO_3$ single crystals. *Applied Physics Letters*, 93(6):061909, 2008.

This thesis was typeset using LaTeX, originally developed by Leslie Lamport and based on Donald Knuth's TeX. The body text is set in 11 point Egenolff-Berner Garamond, a revival of Claude Garamont's humanist typeface. The above illustration, "Science Experiment 02", was created by Ben Schlitter and released under CC BY-NC-ND 3.0. A template that can be used to format a PhD thesis with this look and feel has been released under the permissive MIT (XII) license, and can be found online at github.com/suchow/Dissertate or from its author, Jordan Suchow, at suchow@post.harvard.edu.